Edith Cowan University

Research Online

Research outputs 2022 to 2026

12-1-2023

A comprehensive review on shale studies with emphasis on nuclear magnetic resonance (NMR) technique

Yujie Yuan
Edith Cowan University

Reza Rezaee

Mei-Fu Zhou

Stefan Iglauer
Edith Cowan University

Follow this and additional works at: https://ro.ecu.edu.au/ecuworks2022-2026

Part of the Engineering Commons

10.1016/j.jgsce.2023.205163
Yuan, Y., Rezaee, R., Zhou, M. F., Iglauer, S. (2023). A comprehensive review on shale studies with emphasis on nuclear magnetic resonance (NMR) technique. Gas Science and Engineering, 120, article 205163. https://doi.org/10.1016/j.jgsce.2023.205163
This Journal Article is posted at Research Online.
https://ro.ecu.edu.au/ecuworks2022-2026/3339

120 (2023) 205163

Contents lists available at ScienceDirect

Gas Science and Engineering

journal homepage: www.journals.elsevier.com/gas-science-and-engineering

A comprehensive review on shale studies with emphasis on nuclear magnetic resonance (NMR) technique

Yujie Yuan [a,b,c,d,*], Reza Rezaee [d], Mei-Fu Zhou [e,f], Stefan Iglauer [b,c]

[a] School of Earth Sciences, Yunnan University, Kunming, 650500, China
[b] Centre for Sustainable Energy and Resources, Edith Cowan University, 270 Joondalup Dr, Joondalup, 6027, WA, Australia
[c] School of Engineering, Edith Cowan University, 270 Joondalup Dr, Joondalup, 6027, WA, Australia
[d] Western Australian School of Mines: Minerals, Energy and Chemical Engineering, Curtin University, Perth, 6107, Western Australia, Australia
[e] School of Earth Resources, China University of Geosciences, 430074, Wuhan, China
[f] State Key Laboratory of Ore Deposit Geochemistry, Institute of Geochemistry, Chinese Academy of Sciences, Guiyang, 550081, China

ARTICLE INFO

Keywords:
Shale gas
Nuclear magnetic resonance (NMR)
Multiscale
Multidisciplinary
High-resolution

ABSTRACT

Multi-scale shale studies put a significant emphasis on high-resolution investigations from nanometer to decametre scales. Despite that multiple advanced techniques have been used in shale studies, they are mostly limited to the detection scopes and have restricted capacity for high-resolution characterization of shale nanopores with substantial heterogeneity. Therefore, it remains a challenge for accurate resource estimation in unconventional shales. The nuclear magnetic resonance (NMR) is an advanced technique enabling non-destructive and fast measurements, and has the advantage of high-resolution evaluation of shale formations and nanopore structure. Petrophysical studies using NMR have made breakthroughs in shale studies. However, multi-scale shale investigations with emphasis on NMR technique have not been fully reviewed. This paper thus provides an overview of the capabilities of NMR in multidisciplinary shale studies to largely improve accuracy in unconventional resource estimations. We proposed a multi-scale and quantitative NMR detection method for accurate characterization of the nanopore structure and fast relaxation fluids. The laboratory NMR core analysis and NMR well logging can be applied for the detection from nanometer to decametre scales, respectively, and precisely measure shale reservoir properties, including total/effective porosities, clay-bound water (CBW) contents, pore size distribution, surface relaxivity, absolute permeability, wettability, and fluid types. Importantly, with NMR application, new research areas such as the integrated supercritical CO_2 enhanced shale gas recovery ($scCO_2$-ESGR) and carbon geo-sequestration, and the advanced underground hydrogen storage (UHS) in shales can be developed to achieve the target of long-term energy supply and net-zero carbon emission. New techniques such as in-situ kerogen pyrolysis are also improved by using NMR dynamic monitoring.

1. Introduction

The urgent demand for a large amount of sustainable energy requires alternative supply trains, and thus stimulates global shale resource investigations (Dong et al., 2018; Jin et al., 2022; Zhang et al., 2017; Zou, 2017). In this context, shales have been identified as a key unconventional resource with a tremendous amount of reserves in the world (Loucks and Ruppel, 2007). However, unlike conventional reservoirs, which have good reservoir properties, e.g. large porosity and permeability, shales are dramatically more complex as they are composed of fine-grained clay- or silt-sized particles (less than 62.5 μm in diameter) with a tight texture and large heterogeneity in petrophysical properties at multiple scales (Folk, 1980; Javadpour, 2009). Low porosity (mostly less than 10 %) and extremely low permeability, and permeability from nD to a few mD are thus commonly observed in shales (Passey et al., 2010). The pore structures, e.g., porosity, pore size distribution (i.e., PSD), pore connectivity, and fluid flow properties are therefore difficult to measure, which limits the full utilization for economic values of shale resources (Fleury and Romero-Sarmiento, 2016).

The success of commercial shale gas/oil production essentially relies on the accurate estimation of the storage capacity and fluid transportability in complex nanopore structures and the dynamic shale reservoir monitoring (Hao et al., 2013; Jin, 2023; Zhang et al., 2021; Zou, 2017). Consequently, it is urgently required to comprehensively

* Corresponding author. School of Earth Sciences, Yunnan University, Kunming, 650500, China.
E-mail addresses: yujieyuan@ynu.edu.cn, y.yuan@ecu.edu.au (Y. Yuan).

https://doi.org/10.1016/j.jgsce.2023.205163
Received 31 July 2023; Received in revised form 3 October 2023; Accepted 27 October 2023
Available online 30 October 2023
2949-9089/© 2023 The Authors. Published by Elsevier B.V. This is an open access article under the CC BY license (http://creativecommons.org/licenses/by/4.0/).

understand and accurately evaluate shale systems from both, static and dynamic, perspectives. Despite that there have been multiple techniques (e.g., helium (HE) porosimetry, mercury injection capillary pressure (MICP), gas research institute (GRI), water immersion porosimetry (WIP), dual liquid porosimetry, and small-angle and ultrasmall-angle neutron scattering (SANS/USANS)) applied in shale studies, they are mostly restricted to the detection scales and incapable of a high-resolution characterization of shale nanopores containing fast relaxation fluids. Additionally, large variations are shown in different measurements, whereas no standardized techniques have been established for accurate quantification of shale nanopore structure attributes (Kuila, 2013; Lai et al., 2018).

The Nuclear Magnetic Resonance (NMR) technique has been widely used in diverse fields such as physics (Bloch, 1946; Purcell et al., 1946), medical science (Dixon and Ekstrand, 1982), material science (Smith and Strange, 1996), chemistry (Claridge, 2016), food science (Alberti et al., 2002), oil and gas industry (Liu et al., 2019; Yuan et al., 2018b), carbon capture utilization and storage (CCUS) (Hadian and Rezaee, 2020) and underground hydrogen storage (Aslannezhad et al., 2023; Mahdi et al., 2021). NMR is a non-destructive and fast detection technique (Coates et al., 1999). Importantly, NMR can perform multi-scale investigations from nanometers to decametre scopes, which is extremely critical for reservoir evaluation (Arif et al., 2021; Yuan, 2020). Thus significant efforts were made in NMR logging, NMR imaging, and laboratory NMR core analysis to obtain the above-mentioned shale properties (Dutilleul et al., 2020; Freedman, 2006; Ge et al., 2018; Xu et al., 2019). In recent decades, NMR has attracted more and more attention owing to its benefits for unconventional reservoir characterization and development. For example, conventional core flooding is limited to reflecting nanopore structure, whereas core flooding integrated with NMR allows the direct and real-time monitoring of two-phase fluids dynamic behaviors controlled by pore throats within nanopore structure (Wu et al., 2015).

In this context, it is therefore timely to review NMR capabilities and limitations in terms of multi-scale and high-resolution petrophysical analysis of shales. This review highlighted exclusive NMR advantages in petrophysical analysis and nanopore structure characterization. Advanced NMR application is also proposed to integrate supercritical CO_2-enhanced shale gas recovery and carbon geo-sequestration ($scCO_2$-ESGR) and underground hydrogen storage (UHS) to mitigate global warming, meanwhile, to guarantee a long-term energy supply. Additionally, NMR application is highlighted in the cutting-edge areas of dynamic monitoring the formation and dissociation of gas hydrates, and oil shale in-situ pyrolysis conversion.

2. Laboratory- and log-based systems of NMR technologies

2.1. NMR principals and laboratory low-field NMR core analysis

NMR is a phenomenon that occurs in response to magnetic hydrogen atomic nuclei toward a magnetic field. Like a gyroscope in the earth's gravitational field, the atomic nucleus orients around the direction of an external magnetic field (Bloch, 1946; Purcell et al., 1946). Protons within atomic nuclei have a relatively large magnetic moment, which is an intrinsic quantum property called 'spin'. The physical interaction between spin and external magnetic fields can be detected by NMR. Considering that hydrogen (^{1}H) contains merely one proton and no neutron, and can produce a strong magnetic moment, meanwhile, ^{1}H is abundant in formation fluids (e.g., in water and hydrocarbons), NMR logging and laboratory rock analysis can thus be widely applied in oil and gas industry and scientific research (Coates et al., 1999). The initial amplitude of the spin-echo is proportional to the number of ^{1}H nuclei that are associated with the pores fluids. Thus, this amplitude can be utilized and calibrated to calculate porosity. The echo can be used for data acquisition parameters and the properties of the pore fluids within tested samples. The properties of the pore fluids affecting the echo include the hydrogen index, longitudinal relaxation time ($T1$), transverse relaxation time ($T2$), and diffusivity (D).

To obtain the NMR T_2 spectrum, the raw NMR T_2 data are acquired and inverted using different methods, therefore demonstrating different T_2 performances. In laboratory rock analysis, the Carr, Purcell, Meilboom, and Gill pulse (CPMG) pulse sequence (Carr and Purcell, 1954; Kenyon et al., 1995; Meiboom and Gill, 1958) is employed with appropriate parameters, including inter-echo spacing (TE), inter-experiment delay, number of echoes and signal to noise ratio. In terms of fluids in rock pores, independent $T2$ relaxation mechanisms include surface relaxation, molecular diffusion relaxation, and bulk fluid relaxation (Fig. 1; Eq. 2.1.1). While bulk fluid and molecular diffusion relaxation are negligible effects in a uniform electromagnetic field with short echo spacing carried out on brine-saturated samples (Yuan et al., 2018b), T_2 relaxation can thus be simplified as **Eq. 2.1.2** (Coates et al., 1999).

$$\frac{1}{T_2}=\frac{1}{T_{2bulk}}+\frac{1}{T_{2surface}}+\frac{1}{T_{2diffusion}} \tag{2.1.1}$$

$$\frac{1}{T_{2\text{surface}}}=\rho\left(\frac{S}{V}\right) \tag{2.1.2}$$

where ρ is the surface relaxivity, μs/m; $\frac{S}{V}$ is the specific surface area of the pore (the ratio of surface area to pore volume), μs^{-1}. What is worth mentioning, surface relaxivity is related to the rock mineralogy, particularly, paramagnetic minerals such as pyrite and siderite in shales have a dramatic influence (Yuan and Rezaee, 2019c).

Additionally, the Magic Sandwich Echo (MSE) pulse sequence has been suggested for certain circumstances (Yan et al., 2018). There are four T2 inversion algorithms available, including non-negative least squares (NNLS-LH) with L-curve (Lawson and Hanson, 1995), generalized cross-validation (GCV) (Golub et al., 1979), Butler-Reed-Dawson (BRD) (Butler et al., 1981), and UPEN (Borgia et al., 1998). Regarding shale analysis, NNLS-LH and GCV perform better than the other two (Testamanti and Rezaee (2018)).

2.2. NMR logging and magnetic resonance imaging logging (MRIL)

NMR logging enables an in-situ and consecutive measurement of reservoir characteristics at decameter-scale; and this tool is thus widely used in formation evaluation (Coates et al., 1999). Commercial NMR-logging tools were introduced in the early 1980s, but it only became popular with the advent of NUMAR's MRIL. Magnetic Resonance Imaging Logging (MRIL) was a representative NMR Logging tool and was initially introduced by NUMAR in 1991 (Coates et al., 1991). MRIL contains a centralized permanent magnet, which generates an oscillating magnetic field that magnetizes formation materials. NMR logging tools detect a signal from pore fluids only (and no signal from the rock matrix) (Xiao et al., 2016; Yu et al., 2017). Therefore, NMR logging can more accurately detect pore fluids and pore structures than neutron, density, and acoustic logging (Rezaee, 2015). The key formation information collected by NMR logging includes (i) fluid quantities (Prammer et al., 1995); (ii) fluid properties (e.g., fluid type, fluid viscosity, saturation) (Freedman et al., 1997); and (iii) the properties of complex pore structures (e.g., free fluid porosity, bound fluid volume, permeability, pore size distribution) (Labani et al., 2010; Yu et al., 2017).

Despite the multiple advantages of NMR logging outlined above, it was highly restricted due to high expenses and non-usability in cased production wells (Labani et al., 2010). To remedy this, intelligent techniques (e.g., Neuro-Fuzzy (NF) technique (Malki and Baldwin, 2002), Fuzzy Logic and Genetic Algorithms (Ogilvie et al., 2002), Committee Machine with Intelligent Systems (CMIS) model (Kadkhodaie-Ilkhchi et al., 2009), Back Propagation Neural Network (Bhatt and Helle, 2002), Evolutionary Computing (Tamhane et al., 2000),

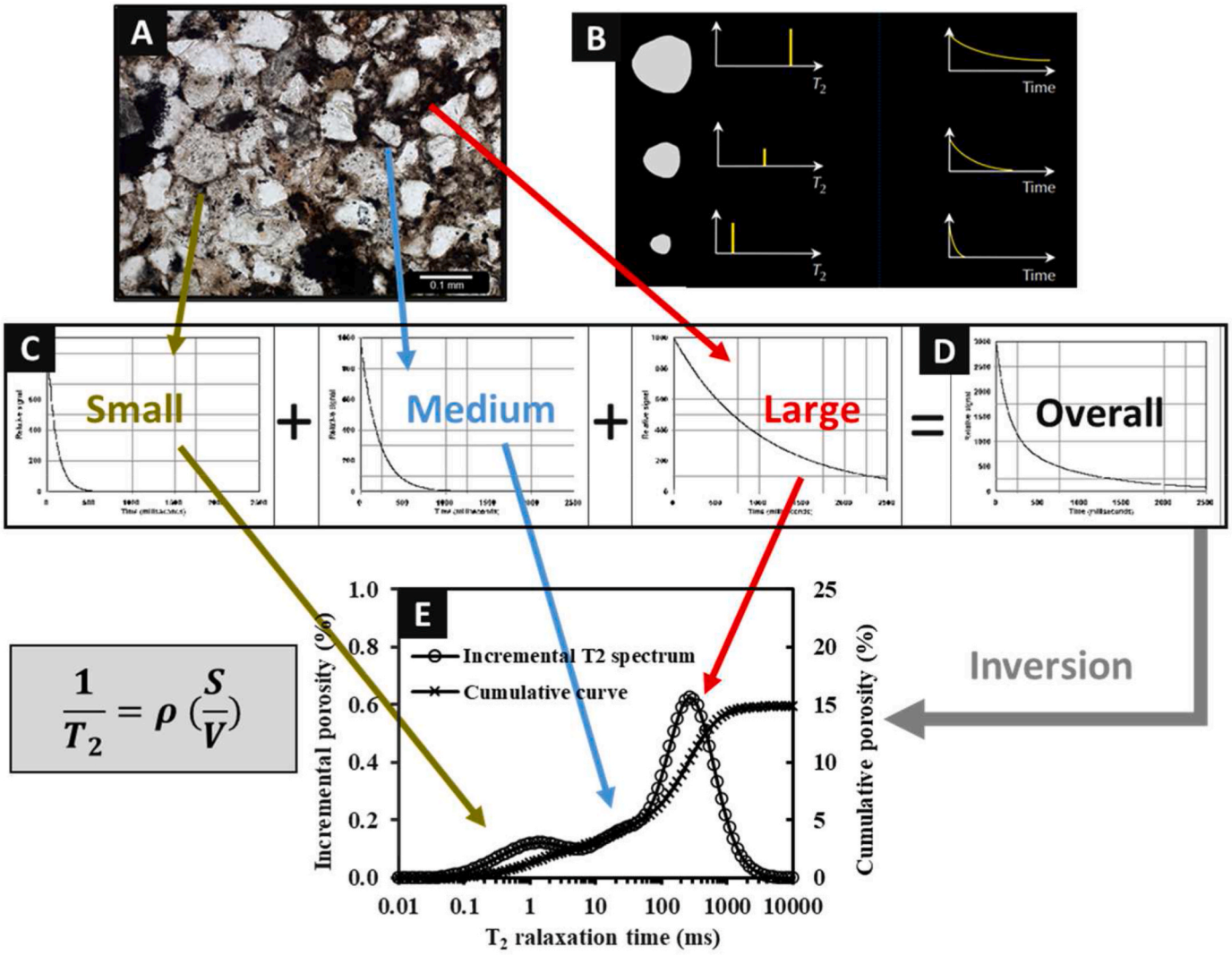

Fig. 1. Inversion of NMR raw T2 data into T2 spectra and pore size distributions. (A) Thin-section image including pores of small, medium, and large sizes; (B) fully-saturated single pores (in small, medium, and large pore size) and their single NMR T2 peaks (C) the corresponding single-exponential decay functions of small, medium, and large pores; (D) fully-saturated complex multi-pore system with multi-exponential decay; (E) incremental and accumulative pore size distributions inverted from Fig.1D.

Takagi–Sugeno FIS (TS-FIS) model (Labani et al., 2010)) were established to overcome these limitations.

2.3. NMR apparatus

NMR apparatus, based on the discussions mentioned above, can be subdivided into (i) benchtop NMR spectroscopy commonly applied in laboratory studies, and (ii) borehole NMR tool employed in geophysical well logging. As summarized in Table 1, the low-field benchtop NMR spectroscopy primarily involves the manufacturers of Oxford Inc., Magritek Inc., Vista Clara Inc., and Niumag Corporation. Different apparatus provides different features regarding resonance frequency, minimum echo spacing (TE), and maximal operating temperature. The borehole NMR tool covers both wireline and logging while drilling (LWD) instruments manufactured by Schlumberger, Halliburton, Baker Hughes, China Oilfield Services Limited, and CNPC Logging Co. Ltd.

3. Applications of NMR in shale studies

3.1. Porosity measurements and the inconsistency of the results between NMR and other approaches

Porosity and pore structure are the most fundamental property of shales for hydrocarbon storage (Hu et al., 2015; Kuila et al., 2014; Tian et al., 2013, 2015, 2016; Yuan et al., 2019). The development of porosity is controlled by the depositional environment, diagenesis, bulk composition, and thermal maturity, and thus reflects a large variation in different shales (Mastalerz et al., 2013; Wu et al., 2015; Cao et al., 2018; Xu et al., 2021). Marine shales commonly demonstrate a higher porosity and a wider porosity range than transitional and continental shales (Fig. 2). To measure porosity of such unconventional shale, various approaches have been used, such as NMR (Liang et al., 2020; Yan et al., 2018), helium (HE) (Furmann et al., 2016), mercury (Hg) porosimetry (Bustin et al., 2008b), Gas Research Institute (GRI) (Luffel and Guidry, 1992; Sondergeld et al., 2010), water immersion porosimetry (WIP) (Kuila et al., 2014), dual liquid porosimetry (Topór et al., 2016), and small-angle and ultrasmall-angle neutron scattering (SANS/USANS) (Liu et al., 2019c; Mastalerz et al., 2012; Sun et al., 2020). The most critical and ambiguous issue, however, is the inconsistency between NMR and

Table 1
Main features of the commercial benchtop NMR instruments. Some data were obtained from previous research (Ge et al., 2021).

	Trademark	Manufacture	Resonance frequency (MHz)	Minimum TE (ms)	Sample diameter (cm)	Maximal temperature (∘C)	Measuring parameters
Benchtop NMR Spectroscopy Tool	GeoSpec 2	Oxford	2, 12, 20	0.06	2.54–15.24	100	T1, T2, T2-D, T1-T2,2D imaging
	MARAN Ultra		2, 23	0.2	2.54		T_1, T_2, T_1-T_2,
	Magritek	Magritek	2, 25, 43	0.06	2.54–3.8		T_1, T_2, T_2-D, T_1-T_2
	MesoMR	Niumag	12, 23	0.06	2.54	120	T_1, T_2, T_1-T_2
	MicroMR	Niumag	2, 12, 20	0.06	2.54		T_1, T_2, T_1-T_2
	Helios	Vista Clara	0.485	0.2	3.8–10.2		T_2
	Trademark	**Manufacture**	**Resonance frequency (MHz)**	**Minimum TE (ms)**	**Vertical resolution (cm)**	**Investigation depth (cm)**	**Measuring parameters**
Borehole NMR Logging Tool	CMR-Plus	Schlumberger	2	0.2	15.24, 22.86, 45.72, 76.2	1.27, 2.84, 3.81	T2
	CMR-MagniPHI		2	0.2			T1, T2, T1-T2
	MR Scanner		0.5–1.1	0.45	19.1, 45.7	3.2, 3.8, 5.8, 6.9, 10.2	T1, T2, T1-T2, T2-D
	Provision Plus 675		0.255	0.6	10.16, 25.4, 50.8	38.1	T2
	Provision Plus 825		0.255	0.6	10.16, 25.4, 50.8	43.2	T2
	MR Explorer	Baker Huges	0.45–0.88	0.3	45.7	6.35–11.43	T1, T2, T1-T2, T2-D
	MagTrak		0.35–0.5	0.4		24.9, 33.5, 45.7	T1, T2
	MRIL-P	Halliburton	0.5–0.8	0.6	60.96	36.1–40.9	T1, T2, T1-T2, T2-D
	XMR		0.547–1.183	0.2		3.8–102	T1, T2, T1-T2, T2-D, T1-T2-D
	MRIL-WD		0.5	0.5			T1, T2, T1-T2
	EMRT	China Oilfield Services	0.55–0.96	0.4	24	5.5–11.5	T2
	MRT6910	CNPC Logging Co.	0.5–0.8	0.6	61	17–22	T2, T2-D
	JPY238	Vista Clara	0.25–0.475	0.45	25	23,28	T2
	JPY350			0.6	50	30, 38	T2
	PX350F			0.8	50	25, 30, 34, 38	T2
	PX525F			0.8	50	36, 40, 46, 53	T2
	CMR-Plus	Schlumberger	2	0.2	15.24, 22.86, 45.72, 76.2	1.27, 2.84, 3.81	T2

other measurements (Yuan and Rezaee, 2019a). Currently, no standardized guideline has been established to systematically explain this inconsistency. Here we used shale samples of nine different formations, including Western Australia, the USA, and China to investigate the essential reason of the porosity discrepancy between NMR and other measurements.

Our results reveal that shale lithofacies are intimately associated with the porosity inconsistency between NMR and other measurements, which is tightly linked to clay-bound water (CBW) developed in shales (Yuan, 2020). CBW is defined as the electrochemically bound water within a clay lattice, or near a pore surface within the electrical double layer. CBW would reduce effective porosity and is largely associated with the properties of pore surface and pore volume in shales, therefore, CBW performs as a critical parameter for accurate estimation of producibility (Yuan et al., 2018b). CBW shows larger amounts in shales with high content of clay minerals (particularly in low-mature shales containing higher contents of smectite); in contrast, less CBW is presented in shales with low clay contents and low TOC. On top of our previous research, further intimate correlations can be found between CBW and shale lithofacies.

Shale lithofacies are classified into four major types: (i) argillaceous (AR), (ii) siliceous (SI), (iii) calcareous (CA), and (iv) mixed lithofacies, based on ternary mineralogy diagram obtained from XRD mineralogical analysis (Liu et al., 2019a). Large lithofacies variations are shown between different shales (Fig. 3A, the detailed mineralogical composition is shown in the pie chart as Appendix content Fig. A). For example, Goldwyer shales are classified as AR lithofacies that are distinguished by extraordinarily high clay contents (avg. > 65%) (Fig. 3A, Fig. A). Carynginia, Wufeng-Longmaxi (O_3w-S_1l), Qiongzhusi, and the shale from Ningtiaota and Jiahe (NT & JH), are mixed lithofacies, containing a moderate combination of clay and quartz content (e.g., the avg. clay content in Carynginia, Wufeng-Longmaxi, Qiongzhusi, and shales from N&J is 36.2 wt%, 40.2 wt%, 31.4 wt%, and 44.5 wt%, respectively; whereas the avg. quartz content is 46.5 wt%, 45.3 wt%, 34.4 wt% and 39.8 wt%, respectively) (Fig. 3A, Fig.A). In contrast, Middle Bakken and Lucaogou shales are categorized into CA lithofacies with a high content of calcareous minerals and very low clay content (e.g., avg. carbonate content in Middle Bakken and Lucaogou shales is 56.4 % and 33.5 %; whereas clay content is merely 6.9 and 8.9 %, respectively) (Fig. 3A, Fig. A). Monterey shales and Bakken shales are SI lithofacies characterized by a very high content of siliceous minerals (e.g., avg. quartz content in Monterey and Bakken shales is 57.0 % and 65.3 %, respectively).

Porosity values obtained from low-field NMR and HE porosimetry are shown in Fig. 3B. Cross-plots of the NMR-HE porosity (φ) for all the samples from nine units reveal that NMR-HE φ discrepancy is highly related to shale lithofacies (Fig. 3B). A favorably equal φ between NMR and HE is commonly demonstrated in clay-poor and OM-poor shales including the CA OM-poor lithofacies (e.g., Lucaogou shales, Middle Bakken shales), and the mixed/SI OM-poor lithofacies (e.g., the Goldwyer shale samples at the depth of 1576.50 m, Fig. 4E). However, a tremendous NMR-HE φ discrepancy is always present in clay-rich and OM-rich shales such as the AR lithofacies (e.g., most of the studied Goldwyer shales), whereas a mild NMR-HE φ discrepancy was found in lithofacies such as the CA OM-rich (e.g., the Goldwyer shale samples at the depth of 1546.14 m, Fig. 4B), and the mixed lithofacies (e.g., Carynginia, Wufeng-Longmaxi, and NT& JH shales, Fig. 3B).

What is worth mentioning, apart from the intrinsic factor of shale lithofacies (mineralogical and organic components), the key factors leading to the NMR-HE φ discrepancy also include the kinetic molecular diameter of the penetrating fluid applied during the laboratory measurements (Yuan and Rezaee, 2019a). However, the impact of kinetic molecular diameter on NMR-HE φ discrepancy can be neglected because the laboratory NMR and HE tests use H_2O and He as the detective molecular probes, respectively, while these molecular probes have similar

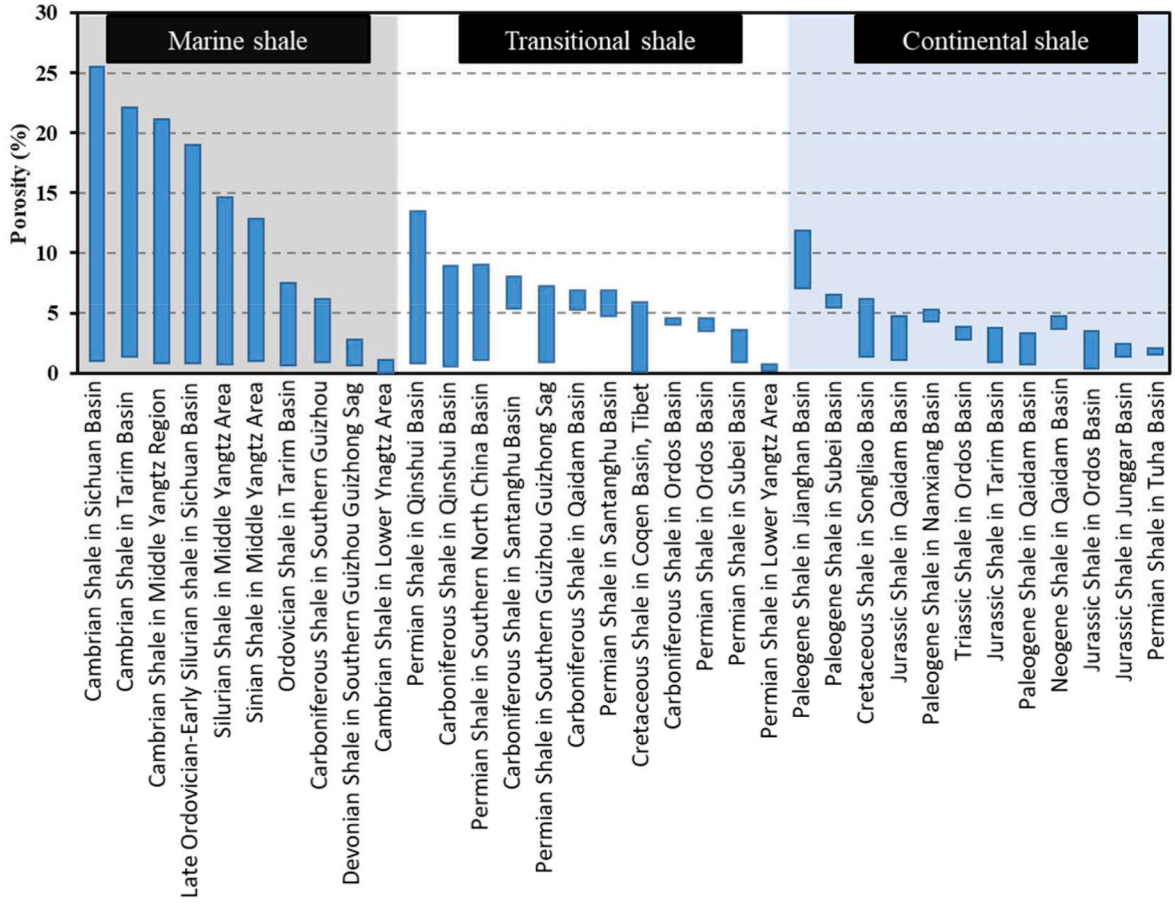

Fig. 2. Porosities of the typical shale formations in China (reproduced from Zhang et al., 2017).

diameters (e.g., the kinetic diameter of H_2O and He are 0.278 and 0.280 nm, respectively, Fig. 3C). Therefore, the NMR-HE φ discrepancy can be considered to be primarily attributed from the intrinsic factor of shale lithofacies, which mainly involves CBW and OM components (Fig. 4).

3.1.1. Comparison of HE porosimetry and NMR

To investigate the mechanism of NMR-HE φ discrepancy, more details of the two techniques should be revealed. HE porosimetry is generally measured using an AP-608 automated porosimeter following the principles of Boyle's law. HE porosimetry detects interconnected porosities, which is equivalent to effective porosity because the working fluid (He) can penetrate the pore structures. The technical steps of HE porosimetry involve (1) the measurement of bulk volume (V_{bulk}) following the Archimedes Method; and (2) the measurement of grain/skeleton volume (V_{grain}). Grain density was determined ranging between 2.6 and 2.7. Fig. 5 presents the mechanism diagram involving initial conditions and equilibrated conditions. The PV value for the whole system before and after switching the valve remains stable per Boyle's Law, which can be expressed in Eq. 3.1.1:

$$P_1\left(V_1 - V_{grain}\right) + P_2V_2 = P_3\left(V_1 + V_2 - V_{grain}\right) \tag{3.1.1}$$

The grain volume is calculated as Eq. 3.1.2:

$$V_{grian} = \frac{P_1V_1 + P_2V_2 - P_3(V_1 - V_2)}{(P_1 - P_2)} \tag{3.1.2}$$

Helium porosity is determined using Eq. 3.1.3:

$$\phi = \frac{V_{bulk} - V_{gain}}{V_{bulk}} \tag{3.1.3}$$

where P_1 is the pressure (atmospheric) within chamber 1 at initial conditions; P_2 is the injected helium pressure within chamber 2 at initial conditions; P_3 is the equilibrated pressure of the system with the valve on. V_1, V_2, V_{grain} are the volume of chamber 1, chamber 2, and the tested samples, respectively.

In contrast, NMR detects hydrogen protons within the pore water and is thus used to obtain the signals from both, penetrated water and CBW, that collectively constitute total porosity. Low-field NMR relaxometry can be used to observe signals from OM apart from CBW (Kausik et al., 2017). It is thus reasonable to assume that the φ gap between NMR and HE is related to the signals from CBW and hydrogen of OM. This is also consistent with our novel discovery of the relationship between lithofacies and NMR-HE φ discrepancy in shales. For example, CA OM-poor lithofacies, e.g., Lucaogou shales, and Middle Bakken shales (Fig. 3 B), contain fewer clay minerals and OM, thus resulting in trace CBW and hydrogen in OM, and demonstrating trace NMR-HE φ discrepancy (Fig. 4). By contrast, AR OM-rich lithofacies contain a large amount of clays and OM, thus leading to a large NMR-HE φ discrepancy.

3.2. Pore size distribution (PSD) and surface relaxivity determination

To obtain PSD from NMR T_2 spectra, a conversion coefficient called transverse surface relaxivity (SR) (Eq. 3.2.1) is commonly used. Surface relaxivity is a parameter to characterize the strength of relaxation induced between solid and fluid interface, and performs as the most significant fitting parameter to convert the NMR signal to length scale and it requires benchmarking with other experiments (e.g., MCIP) (Sigal, 2015). Industry practice generally considers SR as a constant value for the entire formation, whereas SR varies tremendously in shales of different lithofacies (Dunn et al., 2002; Fleury, 2007; Saidian et al., 2015). Surface relaxation of shales is largely impacted by (i) magnetic

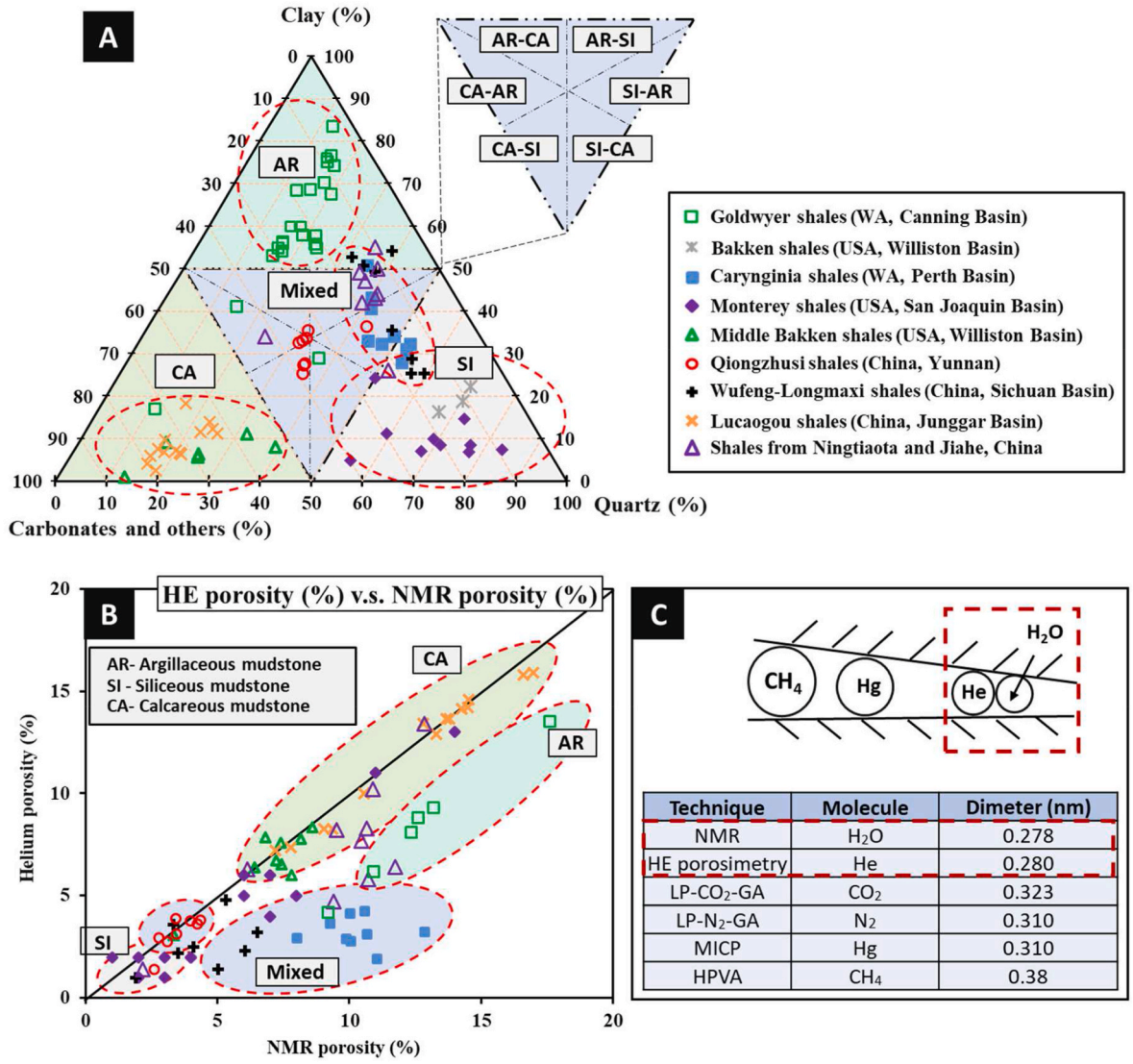

Fig. 3. (A) Ternary diagram of the XRD mineralogical composition and (B) NMR-HE porosity discrepancy of various shale samples. The lithofacies of the studied shale samples include: (i) AR lithofacies- Goldwyer shales (Yuan et al., 2021a, 2023); (ii) CA lithofacies- Middle Bakken Fm. Shales (Karimi, 2017), Lucaogou Fm. Shales (Zhao et al., 2017); (iii) SI lithofacies- Monterey shale (Rivera, 2014), and Bakken shale (Yuan et al., 2021a); (iv) Mixed lithofacies: Qiongzhusi Fm. Shales (Li et al., 2017), Carynginia, Wufeng-Longmaxi (O_3w-S_1l) Fm. Shales (Zheng et al., 2019b), Ningtiaota (NT) and Jiahe (JH) (Zhang et al., 2018); and (C) Schematic model of shale nanopore structure that is analyzed using different penetration molecule probes (e.g., NMR approach using H_2O and helium porosimetry using He), and the kinetic diameter of different molecules (Bustin et al., 2008a). Acronyms: AR = argillaceous, CA = calcareous, SI = siliceous, He = helium, NMR = nuclear magnetic resonance, LP–CO_2–GA = low-pressure CO_2 gas adsorption, LP-N_2-GA = low-pressure N_2 gas adsorption, MICP = mercury injection capillary pressure, HPVA = high-pressure volumetric analyzer, Fm. = formation.

minerals with a high degree of magnetic susceptibility, (ii) Fe-bearing paramagnetic minerals, and (iii) pore surface area to pore volume ratio (SVR) (Hurlimann et al., 1994; Keating and Knight, 2012). Fe-bearing paramagnetic minerals (e.g., pyrite, siderite) have unpaired electrons with randomly oriented spins, and thus induce a faster surface relaxation rate and lead to a higher SR value (Keating and Knight, 2010).

To determine surface relaxivity in conventional reservoirs and coal, several laboratory methods were established (Kleinberg, 1996; Ausbrooks et al., 1999; Slijkerman et al., 2001) following the NMR principle shown in Eq. 3.2.1:

$$\frac{1}{T_{2i}} = \rho_2 \left(\frac{S}{V}\right)_i = \rho_2 \left(\frac{C_s}{r_i}\right) \tag{3.2.1}$$

where T_{2i} is the transverse T_2 relaxation time at experimental point i, ρ_2 is the surface relaxivity, $\left(\frac{S}{V}\right)_i$ is the ratio of pore surface area to pore volume ratio (SVR) that can be determined by low-pressure gas adsorption experiment; r_i is the pore radius at experimental point i; C_s is a shape factor-a constant value dependent on geometric pore shape. Slit, cylindrical and spherical pores correspond to values of 1, 2 and 3, respectively (Zhang et al., 2018).

However, studies of shales revealed a large SR variation, which is associated with lithofacies (Table 2). Shale SR values demonstrated an intimate correlation with Fe-bearing paramagnetic minerals such as pyrite, siderite, and clays that contain high Fe ion concentrations. For shales containing higher Fe ions, the paramagnetic minerals highly influence the NMR response. NMR-converted PSD thus presents divergent shifts off the PSD distribution measured in laboratory. Therefore, attention should be fully concentrated on PSD conversion by considering SR values in the shale, particularly for the shales with a high content of paramagnetic minerals.

Here, we demonstrate the example of shales (e.g., AC1-AC8) from the Permian Carynginia formation in Western Australia. The SR values were calculated based on the logarithmic mean value of NMR T_2 ($T_{2,lm}$) and

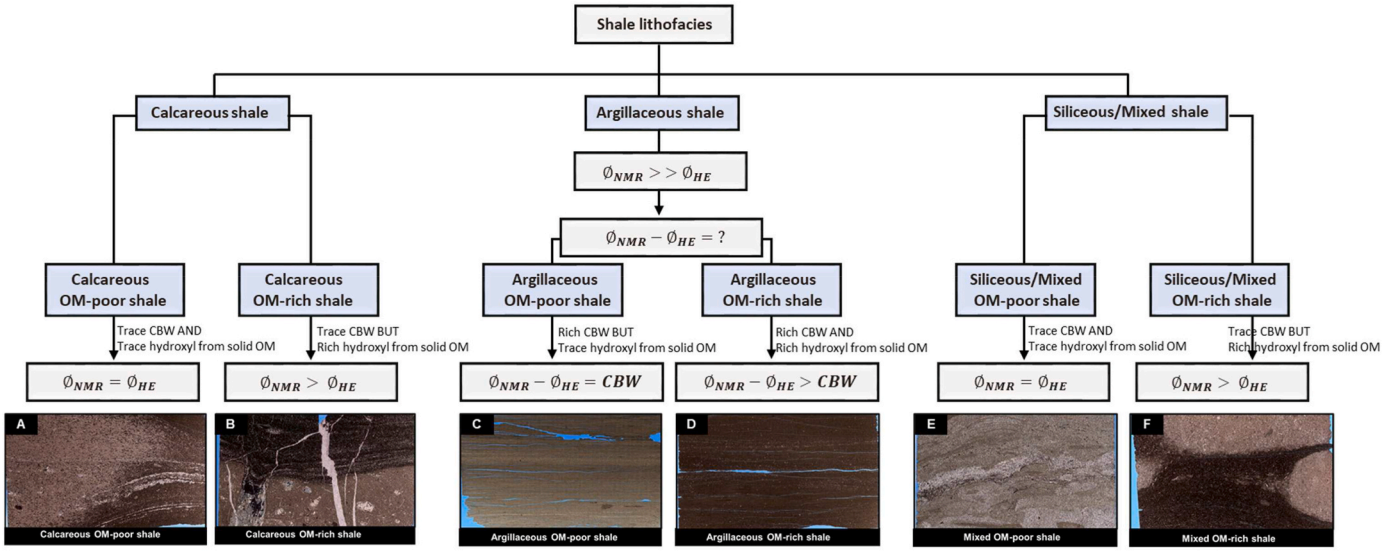

Fig. 4. Relationship between shale lithofacies and NMR-HE porosity discrepancy. Thin sections are Goldwyer samples: (A) calcareous OM-poor lithofacies, from the depth of 1558.26 m, (B) calcareous OM-rich lithofacies, from the depth of 1546.14 m, (C) argillaceous OM-poor lithofacies, from the depth of 1479.76 m; (D) argillaceous OM-rich lithofacies, from the depth of 1559.64 m; (E) mixed OM-poor lithofacies, from the depth of 1576.50 m; (F) mixed OM-rich lithofacies, from the depth of 1547.07 m. Note that the applied lithofacies classification follows the criteria from Yuan et al. (2021a).

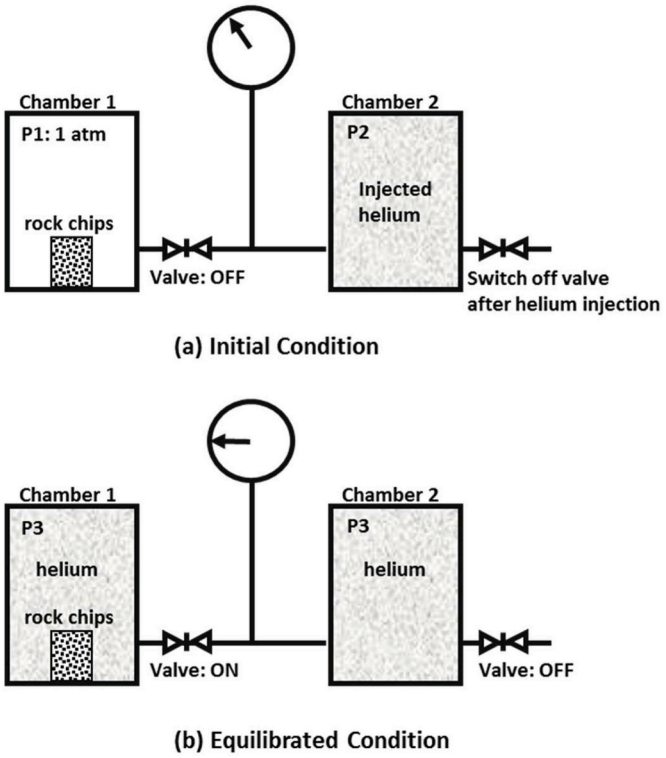

Fig. 5. Diagram of using Boyle's Law to obtain grain/skeleton volume.

the surface-to-volume ratio (SVR) obtained from low-pressure nitrogen gas adsorption (LP-N_2-GA) (Yuan and Rezaee, 2019c). As shown in Table 3, AC1 and AC2 have higher contents of Fe-bearing paramagnetic minerals (e.g., pyrites and clays) and larger SSA (5.53 and 5.57 m^2/g, respectively), presenting higher values of SR (0.25 and 0.29 μm/s, respectively). In contrast, AC8 shows relatively low paramagnetic minerals and low SSA (3.79 m^2/g) and exhibits a low SR value of 0.08 μm/s. Comparing the peaks between the NMR T_2 spectrum and the converted PSD, it is evident that the converted PSD in AC1, AC2, and AC5 shift towards the right; and separate themselves from AC3, AC4, AC8 (Fig. 6). The obvious PSD separations result from the expeditation of the surface relaxation rate, as AC1, AC2 and AC5 show higher Fe-bearing paramagnetic mineral contents and larger SSA. The paramagnetic mineral of higher content expedites the NMR T_2 surface relaxation rate, leading to the divergent shifts in NMR-converted PSD curves.

Table 2
Surface relaxivity of shales, clays, mineral mixtures, and coal.

Rock	Surface relaxivity, ρ (μm/s)	Reference
Permian Carynginia shale	0.08–0.32	Yuan and Rezaee (2019c)
Monterey shale	1–6	Rivera (2014)
Middle Bakken and Three Forks formation shales	0.39–2.54	Saidian and Prasad (2015)
Ordovician XXX OM-rich shale	0.5–3.1	Sulucarnain et al. (2012)
Lower Silurian Longmaxi shale	4.26–28.22	Liu et al. (2018)
Illite	0.9	Prammer et al. (1996)
Smectite	0.9	
Chlorite	0.4	
Pyrite mixture (High-concentration)	1.80	Keating and Knight (2010)
Pyrite mixture (Low-concentration)	1.20	
Siderite mixture (High-concentration)	≥26	
Siderite mixture (Low-concentration)	≥19	
Coal	1.6 (high-rank); 2.1 (low-rank); 3.0 (medium-rank)	Zheng et al. (2019a)

3.3. T_2 cutoff and clay-bound water from 1D NMR

NMR is commonly used in conventional reservoirs to quantify different types of pore fluids, i.e., the bulk volume of moveable fluids, capillary-held water (CHW), and the irreducible clay-bound water (CBW) within pore spaces (Coates et al., 1999; Dunn et al., 2002). T_2 cutoff is the value applied to differentiate these three fluid types for petrophysical analysis. Two threshold T_2 cutoffs, namely T_2 cutoff-1

Table 3
Petrophysical properties of the tested shale samples in Permian Carynginia formation, Western Australia (Yuan and Rezaee, 2019c).

Sample	Depth (m)	Total clay (wt. %)	Pyrite (wt. %)	NMR total porosity, Φ (%)	SSA (m^2/g)	SVR (μm^{-1})	Magnetic susceptivity ($\times 10^{-6}$ SI)	Surface relaxivity ρ (μm/s)
AC1	2780.2	50.8	3.3	10.06	5.53	85.57	63–18,600	0.25
AC2	2781.7	43.2	2.9	10.04	5.57	663.1		0.29
AC3	2789.9	32.3	2.1	11.50	5.18	332.0		0.32
AC4	2794.4	31.1	2.1	10.66	2.84	765.7		0.11
AC5	2806.4	40.7	3.1	12.87	4.28	844.1		0.21
AC8	2825.3	32.3	2.1	8.02	3.79	753.1		0.08

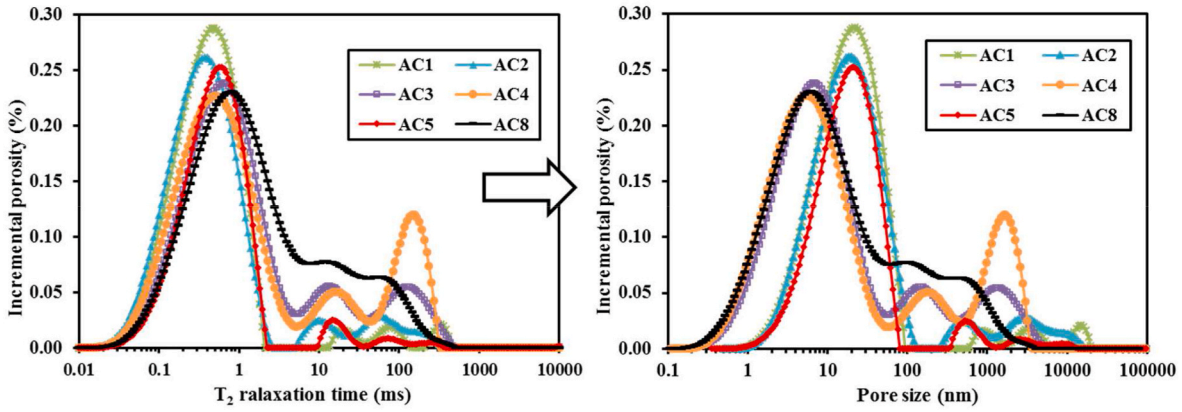

Fig. 6. NMR T_2 spectrum and the converted pore size distribution (PSD) of Permian Carynginia shales in Western Australia (Yuan and Rezaee, 2019c).

($T_{2\text{-}C1}$) and T_2 cutoff-2 ($T_{2\text{-}C2}$), were defined to separate the CHW from the movable volume, and the CBW from CHW, respectively (Fig. 7 C).

To differentiate different fluids and determine T_2 cutoff, an NMR measurement is performed on core plugs under two conditions, one at $S_w = 100\%$ (fully brine saturated condition) and one at S_{ir} = irreducible (residual brine condition after centrifuging) (Xiao et al., 2018; Yao et al., 2010). T_2 cutoff is then obtained by horizontally projecting the peak of the cumulative S_{ir} curve and intersecting with the cumulative S_w curve, followed by projecting down from the intersection point to the x-axis for the T_2 cutoff value (Fig. 7 C).

However, using a centrifuge for fluid partitioning in sandstone, carbonate, or coal is not adaptable for shales (Freedman, 2006; Kenyon, 1992; Straley et al., 1997; Yao and Liu, 2012). Thus pore water in shale can be hardly extracted by centrifuging due to the tight shale texture (Easley et al., 2007), while higher centrifuge rotation speed could lead to structural destruction of the shale sample (Yuan, 2020). Vacuum oven-heating is therefore preferred to extract pore water, and to obtain T_2 cutoff for CBW quantification in shale (Testamanti et al., 2017; Yuan et al., 2018b). As shown in Fig. 7, a vacuum heating procedure was performed under a temperature sequence from 50 °C to 120 °C, to continuously extract pore water from the shale. By detecting the remaining hydrogen proton within pore water, the NMR T_2 spectrum is obtained to determine T_2 cutoff for CBW (Yuan, 2020).

T_2 cutoff and CBW values vary significantly between different rock types. The value of $T_{2\text{-}C1}$ (the T_2 cutoff-1 to differentiate CHW from movable volume) of sandstone and carbonate is 33 and 92 ms, respectively (Straley et al., 1997), while $T_{2\text{-}C2}$ (the T_2 cutoff-2 to separate CBW from CHW) in sandstone was identified as 3 ms (Prammer et al., 1996). In the tight oil samples from the Candong depression, Bohai Gulf basin, China, $T_{2\text{-}C1}$ and $T_{2\text{-}C2}$ show the value of 0.12 and 6.12 ms, respectively (Yan et al., 2017). T_2 cutoff in shale, however, is largely influenced by lithofacies, e.g., $T_{2\text{-}C2}$ in Carynginia shales lie between 0.17 and 0.26 ms (Yuan et al., 2018b), in Lower Silurian Longmaxi shales between 0.09 and 0.36 ms (Liu et al., 2018).

3.4. Fractal analysis

To quantify the complexity of pore structures of shales, fractal analysis can be carried out on tested samples. The fractal theory was initially put forward to describe the fragmented irregularities of geometric objects (Avnir and Jaroniec, 1989; Mahamud and Novo, 2008; Mandelbrot et al., 1984). Microscopically, the structure of rock also has a property of 'self-similar regularity' that presents a similar structure regularity over three orders of magnitude (Katz and Thompson, 1985). This self-similarity can be quantified by fractal dimension (D), which describes the heterogeneity or complexity of a pore structure (i.e., pore surface and pore volume) in shale (Bu et al., 2015; Yang et al., 2014). As thermal maturity increases, pore structure evolves, leading to a change in fractal dimension (Liu et al., 2019b). Fractal dimension can be determined via NMR, low-pressure gas adsorption (LP-GA), MICP, small-angle and ultrasmall-angle neutron scattering (SANS/USANS), and SEM.

To calculate the NMR fractal dimension, the NMR T_2 spectrum is used coupled with fractal theory, following the relationship between N(r) ~ radius (r) described as Eq. 3.4.1 and Eq. 3.4.2 (Avnir et al., 1984; Mandelbrot et al., 1984):

$$N(r) = \int_r^{r_{max}} f(r)dr = \frac{C}{r^D} \tag{3.4.1}$$

$$f(r) = \frac{d\,N_{(r)}}{dr} = \frac{-D \bullet C}{r^{D+1}} \tag{3.4.2}$$

where r is the radius of the equivalent capillary bundles; N_r is the total number of pores (with pore radii > r); $f(r)$ is the function of pore radius density; C is a fractal factor and D is the fractal dimension. Cumulative pore volume with pore sizes smaller than r (V_r) and total pore volume with full size of pores (V_t) were calculated using Eq. 3.4.3 and Eq. 3.4.4 (Coates et al., 1999). In gas shale of nanometer-scaled pore radius, assuming that $r_{min} \ll r$, we can simplify the ratio of V_r to V_t (V) following Eq. 3.4.5 and Eq. 3.4.6. Considering that NMR theory suggests a proportional relationship between T_2 and pore size, Eq. 3.4.6 was converted

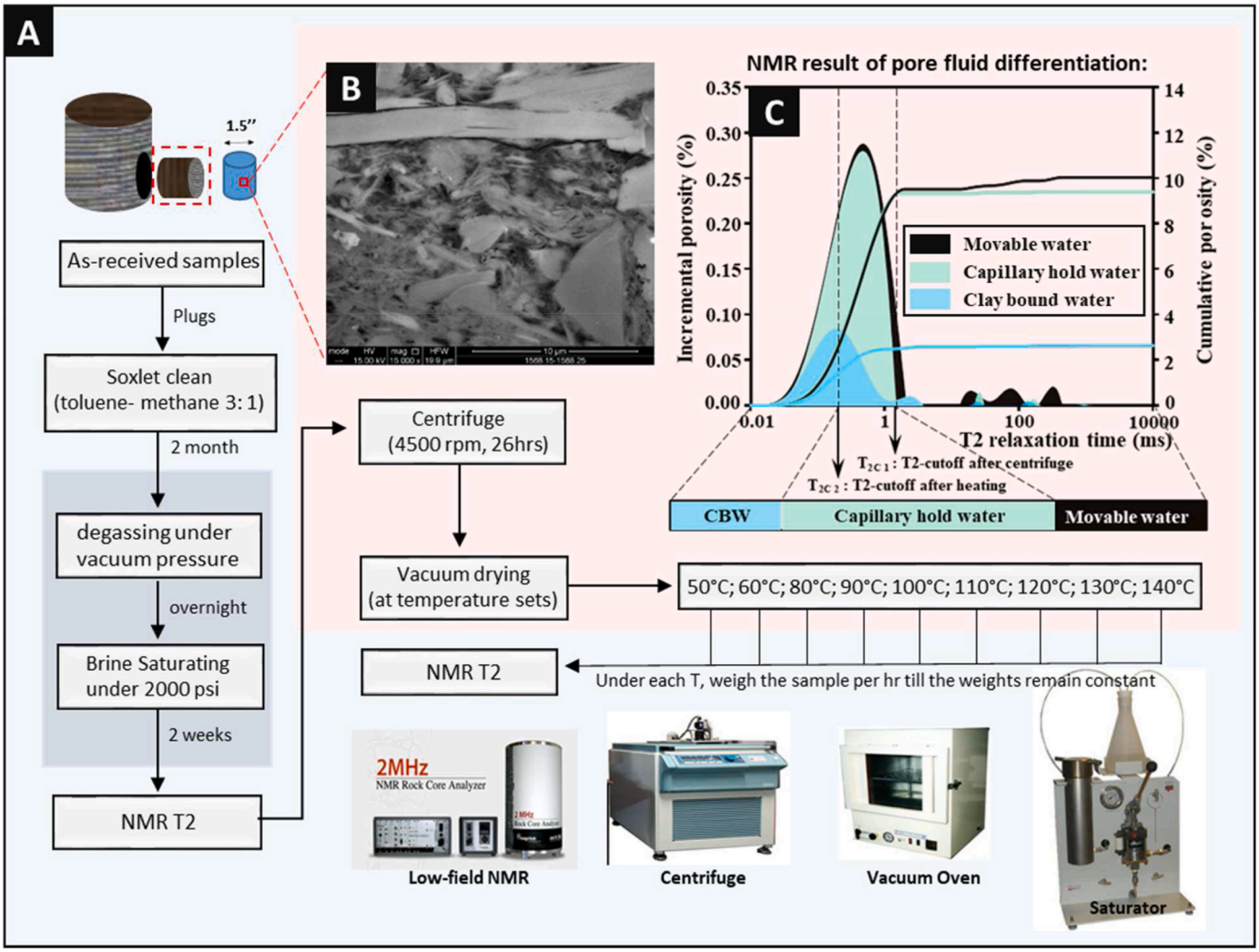

Fig. 7. (A) Workflow to determine $T_{2\text{-cutoff}}$ for CBW quantification in shale (modified from Yuan (2020), Copyright of 2020 Curtin University). (B) SEM image of a representative shale sample; (C) NMR-derived PSD of a representative shale sample (Permian Carynginia shale at depth of 2780.2 m) under three conditions: (i) fully saturated (black), (ii) centrifuged (green), and (iii) Oven-heated (light blue).

into Eq. 3.4.7 and subsequently logarithmetized as Eq. 3.4.8. NMR fractal dimension thus can be obtained as per the slope of the double logarithmic plot shown in Eq. 3.4.8.

$$V_r = \int_{r_{min}}^{r} f(r) c r^3 dr = \frac{-D \bullet C^2}{3-D}\left(r^{3-D} - {r_{min}}^{3-D}\right) \tag{3.4.3}$$

$$V_t = \frac{-D \bullet C^2}{3-D}\left({r_{max}}^{3-D} - {r_{min}}^{3-D}\right) \tag{3.4.4}$$

$$V = \frac{V_r}{V_t} = \frac{r^{3-D} - {r_{min}}^{3-D}}{{r_{max}}^{3-D} - {r_{min}}^{3-D}} \tag{3.4.5}$$

$$V = \left(\frac{r}{r_{max}}\right)^{3-D} \tag{3.4.6}$$

$$V = \left(\frac{T_2}{T_{2\ max}}\right)^{3-D} \tag{3.4.7}$$

$$\log(V) = (3-D)\log(T_2) + (\mathrm{D}-3)\log(T_{2\ max}) \tag{3.4.8}$$

Considering that shale is characterized by complex pore structure and tight texture, the conventional fluid differentiation approach, i.e., centrifuging, poorly works on the determination of T_2 cut-off. Centrifuge rotation higher than 4500 rpm (315 psi) would destroy some of the shales (e.g., Permian Carynginia shals from Western Australia), while centrifuge ≤4500 rpm extracted little water (Yuan et al., 2018b). Take Permian Carynginia shals from Western Australia as an example, as shown in Fig. 7 C, little differences are shown in incremental porosity after the high-speed centrifuge. By applying a pre-heated scheme (heating temperatures range from 50 to 120 °C) on samples before NMR tests, T_2-cutoff was able to be calculated for differentiating various pore types under each temperature. For example, the complexity of effective pores and ineffective pores occupied by CBW in shales can be quantified by the NMR-derived fractal dimension D_{eff} and D_{cbw}, respectively, as NMR enables the differentiation of various pore types containing different fluids (Liu et al., 2021; Yuan and Rezaee, 2019b). The fractal dimension calculated from LP-GA results is intimately associated with the complexity and roughness of micropores, mesopores, and macropores (Mangi et al., 2020). D linearly and positively correlates with clay contents, is related to micro-/mesopore pore geometry, largely complicates the fractal geometry of the nanopore network, and potentially resists effective fluid flows in shales (Yuan and Rezaee, 2019b).

Fig. 8 shows a schematic model of pore surface heterogeneity as the fractal dimension increases from 2 (flat surface) to 2.9 (rough surface) (Shang et al., 2019). For shales abundant in clay minerals, the nanopore surface creates more CBW retention and further reduces the effective

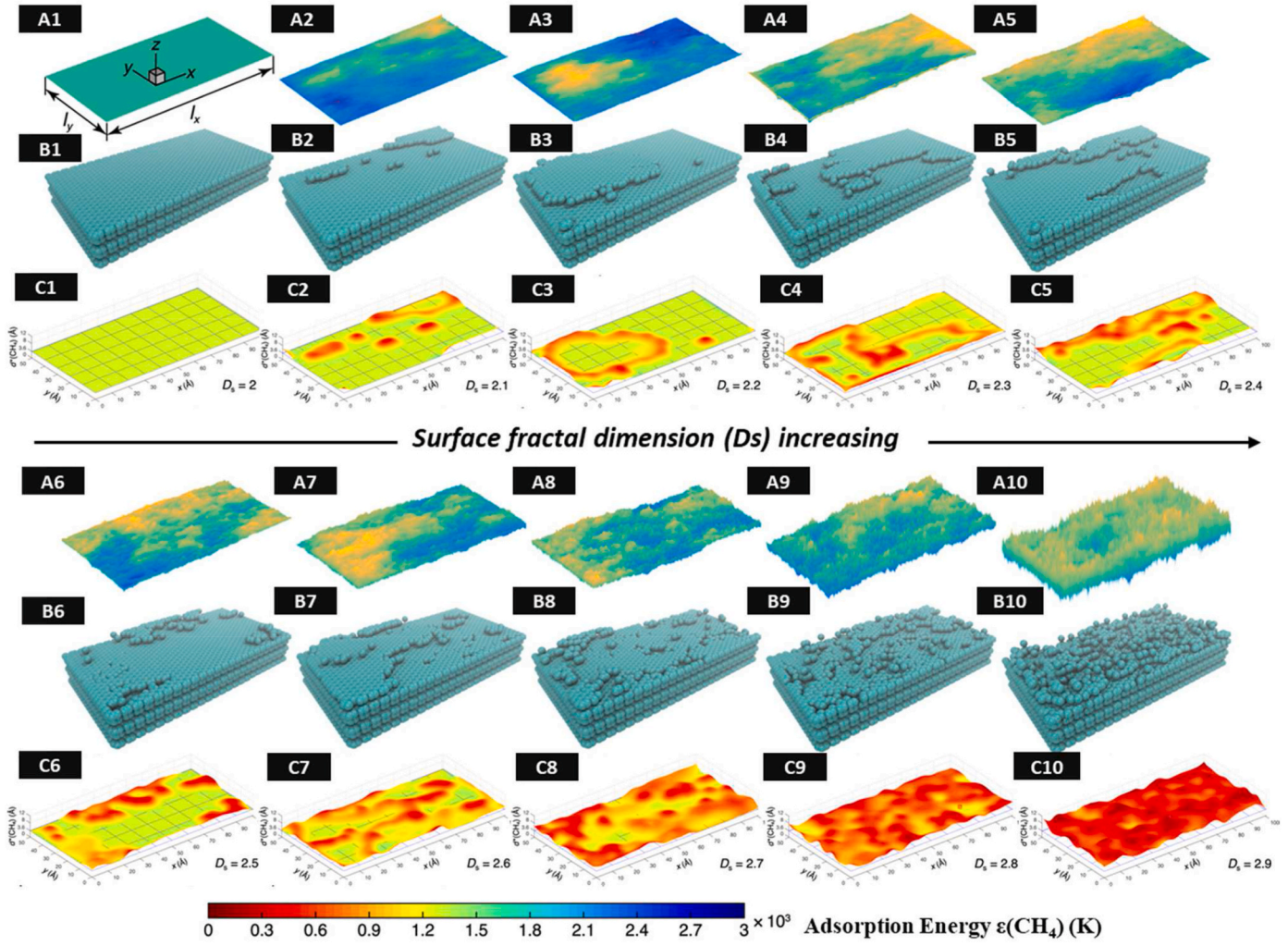

Fig. 8. Schematic model of pore properties as surface fractal dimension (Ds) increases from 2 (flat surface) to 2.9 (rough surface). (A1-A10) Pore surface roughness. (B1–B10) Atomistic models (yellow and blue colors for crests and troughs, respectively). (C1–C10) Correlations between adsorption energy (ε(CH_4), K) and the equilibrium distance (d*(CH_4)) of CH_4 with Ds. Note that the model represents a slit nanopore and is reproduced from Shang et al. (2019).

pore space and thus fluid transport (Zou et al., 2020). More complex meso-/macropores are associated with a larger heterogeneity in effective pores, and have a higher potential of hydrocarbon storage capacity in gas shales (Yuan and Rezaee, 2019b).

3.5. Permeability estimation from 1D NMR

Permeability is the measurement of how easily a gas or a liquid can flow through the pore throats. To quantify the flow of a fluid through a porous medium, Darcy's law can be used following Eq. 3.5.1.

$$u = -\frac{\mathrm{k}}{\mu} \bullet \frac{dp}{dx} \tag{3.5.1}$$

where u is the rate of volume flow across a unit area ($m^3 \cdot s^{-1}\ m^{-2}$), and it is equivalent to mean velocity (m/s) through a porous media. μ is the viscosity, and $\frac{dp}{dx}$ is the pressure gradient in the x direction. Conventional measurements of permeability include: (1) the steady-state permeability method, with a constant pressure gradient, and the permeability is directly proportional to the fluid velocity. (2) the unsteady-state permeability method, which is effective in determining very small permeability, ranging from 0.1 nd to 0.1 μD. It consists in one fluid displacing another one at a previously set rate. The saturation of the core plug/crushed sample will change with time. The unsteady-state permeability method can be subdivided into the oscillating pulse method, the GRI method and the pulse decay method.

Permeability is a fundamental property of shales for fluid flows and is related to the pore geometry (Pan et al., 2015). The pore geometry of shales has large complexity and heterogeneity; it is thus challenging to accurately obtain or predict the permeability of shales. Permeability prediction models established for conventional rock estimations (Table 4) were not available for shales. Thus numerous attempts have been made to better understand shale permeability, however, results have not yet been consistently established. Given that NMR bears the advantage of detecting complex pores at a small pore size scale, permeability estimation obtained from NMR measurements is thus widely acknowledged to produce more precise predictions (Tan et al., 2015).

To estimate absolute permeability based on NMR. Two theoretical models are commonly used: (1) the mean T_2 model, which is also known as the SDR (Schlumberger-Doll-Research) model (Eq. 3.5.2) (Kenyon et al., 1988), and (2) the Coates model (Eq. 3.5.3) (Coates et al., 1998).

$$K_{SDR} = C_{SDR} T_{2gm}^2 \phi_{NMR}^{\ 4} \tag{3.5.2}$$

$$K_{Coates} = \left(\frac{FFI}{BVI}\right)^2 \left(\frac{\phi_{NMR}}{C_{coates}}\right)^4 \tag{3.5.3}$$

Table 4
Permeability estimation models based on NMR and MICP measurements for different lithofacies.

Model	Reference	Sample Lithology
$K_{air} = 339\left(\frac{S_{hg}}{P_c}\right)^{1.691}_{apex}$ $K_{brine} = 355\left(\frac{S_{hg}}{P_c}\right)^{1.691}_{apex}$	Swanson (1981)	Carbonates and sandstones
$log\, r_{35} = 0.732 + 0.588\, log\, K_{air} - 0.864\, log\phi$	Winland equation	Sandstones
$log\, r_{35} = 0.9058 + 0.5547\, log\, K_{air} - 0.9033\, log\phi$	Kolodzie (1980)	Sandstones
$log\, r_{20} = 0.218 + 0.519\, log\, K_{air} - 0.303\, log\phi$ $log\, r_{25} = 0.204 + 0.531\, log\, K_{air} - 0.350\, log\phi$	Pittman (1992)	Sandstones
$log\, K_{air} = -1.160 + 0.930\, log\, r_{50} + 1.780\, log\phi$	Rezaee et al. (2006)	Carbonates
$log\, K_{air} = -1.92 + 2.18\, log\, r_{10} + 0.949\, log\phi$	Rezaee et al. (2012)	Tight gas sandstones
$log\, K_{air} = 0.214 + 2.225\, log\, r_{50}$	Gao and Li (2016)	Tight gas sandstones
$log\, K_{air} = -7.94921 - 0.3829\, log\, r_{55} + 8.9485\, log\phi$	Ngo et al. (2015)	Sandstones
$log\, K_{air} = -2.03939 + 1.2263\, log\, r_{20} + 1.93606\, log\phi$	Ngo et al. (2018)	Carbonates
$log\, K_{air} = -0.588 + 0.842\, log\, r_{10} + 1.559\, log\phi - 1.411\, log\, R_1 + 0.599\, log\, R_2$	Liu et al. (2020)	Shales

K_{air} is the air permeability (mD), S_{hg} is the mercury intrusion volume, P_c is the capillary pressure representing the apex of the hyperbolic log-log Hg injection plot. r_{50} is the pore throat radius at the point of 50% Hg intrusion (μm); R_1 and R_2 are the curvature values, for the intrusion of Hg at larger pores and capillaries, respectively (μm).

$$T_{2gm} = \exp\left(\sum \frac{\ln\,(T_{2i})\phi_i}{\sum \phi_i}\right) \tag{3.5.4}$$

where K is the matrix permeability, T_{2gm} is the geometric mean value of the NMR T_2 spectrum under saturated water condition ($S_w = 100\,\%$). ϕ_{NMR} is the NMR total porosity. T_{2i} is the ith transverse relaxation time (s), and ϕ_i is the incremental NMR porosity corresponding to the i^{th} transverse relaxation time. $\sum \phi_i$ is the total NMR porosity. C_{SDR} is a correction coefficient that is related to the formation type, C_{SDR} is typically determined via calibration with porosity and permeability of core samples (Rezaee et al., 2012). C_{SDR} for sandstone is 4, while 4.75 is suggested for carbonates (Chang et al., 1994). FFI (free fluid index) and BVI (Bound volume irreducible) are the volumes of movable fluid and irreducible bound fluid, respectively, that are detected by NMR.

C_{coates} depends on pore geometry, and is defined as the pore throat to pore body ratio (aspect ratio). Lower aspect ratios (lower C_{coates} values) exhibit more complex geometries and lower permeability indicating higher pressure is required for the fluid to overcome the capillary pressure to flow in the pore structure (Al Hinai, 2014). Given that MICP and NMR are effective approaches to determining pore throat and pore body, respectively, permeability can be estimated using models based on NMR and MICP measurements. Table 4 shows the calculation models for different lithofacies. Note that C_{coates} is typically used to calibrate NMR log analysis from the Coates model. C_{coates} of sandstones is 10, while shales have very low C_{coates} values due to the influence of clays (higher clay contents result in lower C_{coates} values, as they induce a dramatically more complex pore geometry) (Rezaee et al., 2012). Due to this complex pore geometry, shale SDR and Coates models need to be modified by incorporating the NMR pore structure characteristics discussed in sections 3.1 and 3.2, thus Eq. 3.5.5-3.5.8 can be obtained.

$$K_{SDR} = a\,\log\left(T_{2gm}\right) + b\,\log\phi_{NMR} + C_{SDR} \tag{3.5.5}$$

$$K_{SDR} = a\,\log\left(T_{2gm}\right) + b\,\log\phi_{eff} + C_{SDR} \tag{3.5.6}$$

$$\log\, K_{Coates} = a\,\log\left(\frac{FFI}{BVI}\right) + b\,\log\,\phi_{NMR} + C \tag{3.5.7}$$

$$\log\, K_{Coates} = a\,\log\left(\frac{\phi_{eff}}{CBW}\right) + b\,\log\phi_e + C \tag{3.5.8}$$

where ϕ_{NMR} and ϕ_{eff} are the total NMR porosity and the effective NMR porosity, while CBW is the volume of clay-bound water (Yuan et al., 2018b).

However, the modified SDR model can only be used for rocks fully saturated with water, whereas the modified Coates model can also be used for water and hydrocarbon-containing rocks via $T_{2\,cutoff}$ value (Testamanti, 2018). However, $T_{2\,cutoff}$ determination in shale requires complex laboratory analysis (e.g., high-speed centrifuging and vacuum oven-heating (Yuan et al., 2018b)) and experimental conditions largely vary between shale lithofacies. Note that $T_{2\,cutoff}$ derived from the Coates model and T_{2gm} derived from the SDR model deviate greatly, and $T_{2\,cutoff}$ tends to be lower (Rezaee et al., 2012).

3.6. Fluid typing from 2D NMR

Fluid typing plays a critical role in shale reservoir characterization (Li and Cai, 2023; Yuan et al., 2018b). The reservoir quality of shale (particularly oil shale) greatly relies on the amount of light hydrocarbon and natural gas of shale (Chen et al., 2022; Kausik et al., 2016). Apart from hydrocarbons, the formation water is also an important factor for the evaluation of reservoir quality. For example, CBW (as discussed in section 3.1) can drastically reduce effective porosity, thus reducing fluid flow capacity (Yuan et al., 2018a). It is therefore of key importance to differentiate those fluids that are residing in various pore types.

NMR enables the identification of various shale components, such as irreducible fluid and immobile hydrocarbon content (e.g., residual oil, kerogen, bitumen), in the complex pore structure (Fig. 9). Fast-relaxing fluids (such as CBW) in gas shale can be distinguished in 1D NMR T_2 spectra (Yuan et al., 2018b). However, in oil shale, proton signals (between different hydrogen contributions such as bound water and the various forms of hydrocarbons) overlap; to this end, 2D NMR T1-T2 correlation maps and T1/T2 ratios allow more accurate identification of different hydrogen fractions (Rylander et al., 2013; Singer et al., 2016). Given oil shale contains more heavy and viscous hydrocarbon in small pores and movable hydrocarbons in larger pores, 2D NMR demonstrates the exclusive advantages in its fluid typing (Kausik et al., 2016). Moreover, it is possible to identify various fluids in different pore types (e.g., organic pores (OP) and inorganic pores (IP) including interparticle pores and intraparticle pores) and it is also capable of detecting geochemical properties of OM (Khatibi et al., 2019).

Fig. 10A summarizes fluid typing via 2D NMR mapping; it is worth mentioning that the fluid signal patterns exhibit different scenarios between low-frequency and high-frequency NMR, owing to the dependence of T1 on Larmor frequency. The hydrogen protons can be categorized into ① hydrogen protons located at T2 < 0.1ms in both low- and high-frequency 2D NMR maps. ② solid bitumen and kerogen fast relaxation - bitumen in high-frequency NMR is at T1/T2∼100, whereas for low-frequency NMR it is at 4 < T1/T2 < 15. The kerogen signature largely depends on thermal maturity and thus exhibits a large variation between different shales (Xiao et al., 2015). For example, Bakken shale kerogen has a higher T1/T2 when compared to Barnett shale kerogen (T1/T2 in Bakken and Barnett shales is ∼1000 and 10–100, respectively, under high-frequency NMR (Fleury and Romero-Sarmiento, 2016; Khatibi et al., 2019)). ③ Water can be divided into three subclasses: a)

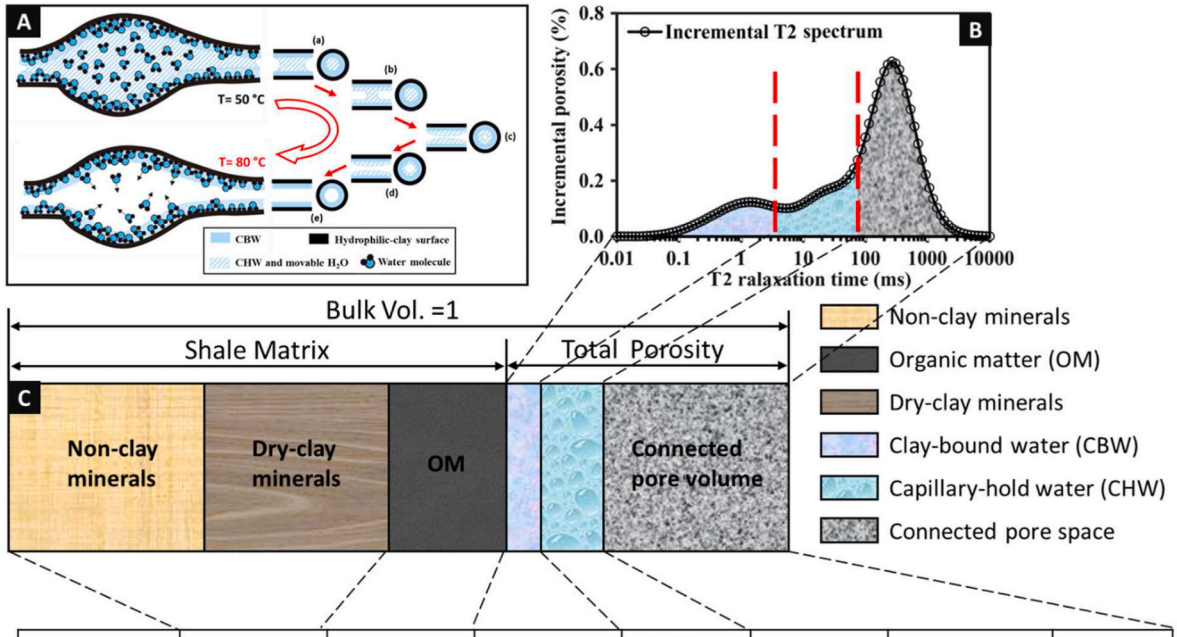

NMR Relaxometry	Structural Hydroxyl	Hydroxyl from OM	Clay-Bound water (CBW)	Capillary-Hold Water (CHW)	Movable Water	Condensate Oil	Gas
T1	Trace signal		Very Short	Short	Medium long	Long	Long
T2	Trace signal	Very Short	Very Short	Short	Medium long	Long	Short
T1/T2 ratio	na	(T2< 0.1 ms)	1-2	1-2	1	1	1
D	na		Slow	Slow	Medium	Medium	Very fast

Fig. 9. (A) The physical model of common pore fluid types (i.e., CBW, CHW, and movable water). (B) The corresponding NMR T_2 spectrum for different pore fluids. (C) Schematic model of petrophysical shale structure and the corresponding NMR relaxometry parameters for different fluid types, modified after (Eslinger and Pevear, 1988) (Coates et al. (1999); Yuan and Rezaee (2019b)).

free water, b) water residing in inorganic pores, and c) clay-bound water with fast relaxation. ④ Hydrocarbons mainly include gas (i.e., free gas, gas in IP, and gas in OP) and oil (i.e., free oil, oil in IP, movable oil in OP, and immovable oil in OP) (Xu et al., 2022).

Fig. 10B, C shows the shales collected from different wells in Goldwyer Fm., Canning Basin, Western Australia. Fig. 10B is a representative shale sample collected from the Theia-1 well at the depth of 1512.7 m in Goldwyer Fm., Canning Basin, Western Australia. Shale samples from this depth are characterized by a very high content of clays (avg. > 65%) and TOC, and tend to present as OM-rich AR lithofacies (Yuan et al., 2023). The 2D NMR map of this shale is distinguished by strong signals of hydroxyls and CBW in IP. In contrast, Fig. 10C is a representative shale sample collected from Cyrene-1 well at the depth of 997.3 m in Goldwyer Fm., Canning Basin, Western Australia. Shales are shown in fewer hydroxyls and CBW in IP.

3.7. Quantitative wettability determination

In a rock containing more than one immiscible fluid (e.g., water and oil), wettability is used as a measurement of the preferential tendency of a certain fluid to wet (spread or adhere to) the rock surface. Thus wettability is defined as "the ability of a liquid to maintain contact with a solid surface in the presence of a third phase" (Anderson, 1986). Wettability is one of the significant parameters for hydrocarbon recovery and the prediction of dynamic fluid flow performance (e.g., for relative permeabilities, production rate, residual oil saturation, imbibition capillary pressure, and oil recovery) (Guo et al., 2022; Iglauer, 2017; Iglauer et al., 2012; Pan et al., 2022). In shales with complex nanopore structures, wettability shows a large heterogeneity and significantly influences dynamic fluid flow and fluid distribution inside the pores, it also affects electrical resistivity (Valori and Nicot, 2019).

To determine wettability, usually conventional wettability measurements (e.g., Amott-Harvey, US Bureau of Mines) are performed; however, NMR has the advantage of being a fast, non-destructive, relatively low-cost benefits, and it allows both, field and laboratory measurements (Ali et al., 2022; Yuan et al., 2021b). Given that the magnetic relaxation rate is positively correlated with the proportion of the surface wetted by the fluid (Brown and Fatt, 1956), wettability can be quantitatively determined by NMR using the wettability index (WI), which is defined as the relative fraction of the surface wetted by water minus that by oil (**Eq. 3.7.1**) (Fleury and Deflandre, 2003; Looyestijn and Hofman, 2006). By introducing WI, Chen et al. (2006) correlated the rock wettability with NMR surface relaxation for Berea cores. For unconventional shale, qualitative wettability analysis was achieved by combining NMR with (oil and brine) imbibition experiments (Odusina et al., 2011; Sigal and Odusina, 2011). This was further quantified (by using WI), which can be determined by modifying **Eq. 3.7.1** into **Eq. 3.7.2** (Sulucarnain et al., 2012). Furthermore, for shales containing abundant residual fluids (such as Eagle Ford shale), a modified equation (**Eq. 3.7.3**) was proposed (Gupta et al., 2019a).

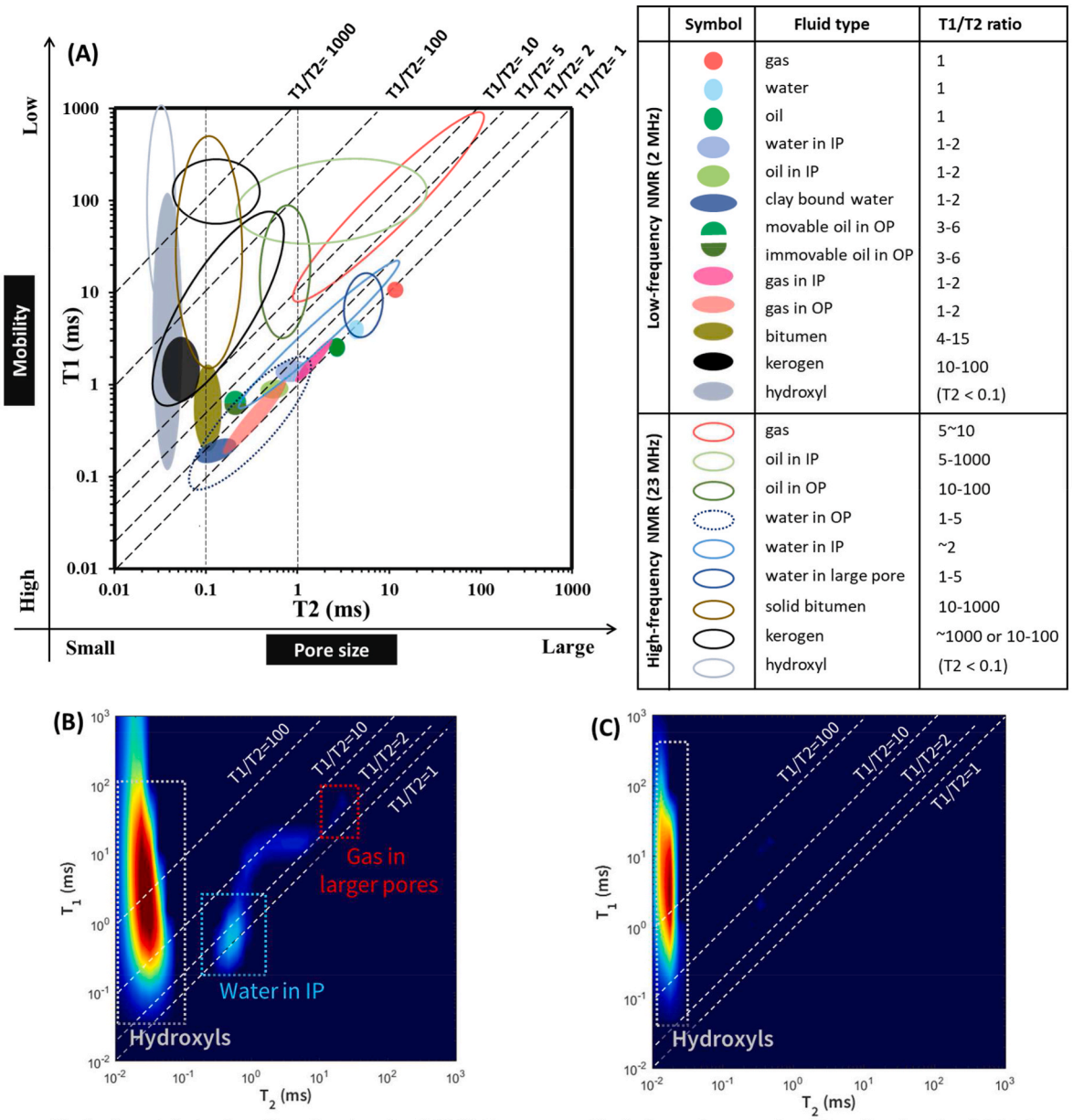

Fig. 10. (A) 2D NMR fluid typing map for shale. Low-frequency NMR (2 MHz) data is modified after Kausik et al. (2016). High-frequency (23 MHz) NMR data is modified after Fleury and Romero-Sarmiento (2016) and Khatibi et al. (2019). (B) An example of a 2D NMR fluid typing map for the shale collected from Theia-1 well at the depth of 1512.7 m in Goldwyer Fm., Canning Basin, Western Australia. The clay content is 55.75 % (illite = 47.8 %) and the TOC content is 2.87 %; (C) An example of a 2D NMR fluid typing map for the shale collected from Cyrene-1 well at the depth of 997.3 m in Goldwyer Fm., Canning Basin, Western Australia. The clay content is 28.70% (illite = 22.92 %) and the TOC content is 1.22 %. Some data were collected from (Testamanti, 2018; Yuan et al., 2021a).

$$WI = \frac{A_w - A_o}{A_w + A_o} \tag{3.7.1}$$

$$WI = \frac{NMR\ (S_w) - NMR\ (S_o)}{NMR\ (S_w) + NMR\ (S_o)} \tag{3.7.2}$$

$$WI = \frac{(NMR\ (S_w) + NMR\ (S_{w,in\ situ})) - (NMR\ (S_o) + NMR\ (S_{o,in\ situ}))}{(NMR\ (S_w) + NMR\ (S_{w,in\ situ})) + (NMR\ (S_o) + NMR\ (S_{o,in\ situ}))} \tag{3.7.3}$$

where WI is the wettability index, ranging from −1 (purely oil-wet) to 1 (purely water-wet). WI from 0 to 1, 0, 0 to 1 represents water-wet, intermediate-wet, and oil-wet, respectively. The value of 0 represents an intermediate-wet (or neutral wettability), indicating no preferential tendency is shown by either fluid towards the rock. WI between −0.5 and 0.5 represents the condition of mixed wettability under the pore-scale perspective (e.g., smaller pores are water-wet, whereas larger pores are oil-wet). Fractional wettability may also be obtained when large heterogeneity occurs in a scattered area (e.g., the scattered area is strongly oil-wet, whereas the rest is water-wet) (Looyestijn and Hofman, 2006). A_w and A_o are the surface areas wetted by water and oil, respectively. $NMR\ (S_w)$ and $NMR\ (S_o)$ is the ratio of the NMR T2 cumulative response of brine and imbibed dodecane to the helium porosity of the sample. $NMR\ (S_{w,in\ situ})$ and $NMR\ (S_{o,in\ situ})$ represent the NMR

responses of residual brine and hydrocarbon, respectively. Note that shale wettability shale demonstrates a large heterogeneity at core scale, Table 5.

3.8. NMR aligned with core flooding for CCUS and EOR/EGR

Carbon capture, utilization and storage (CCUS) has emerged as a significant technology to combat climate change by reducing greenhouse gas emissions. The efficiency of CO_2 geosequestration initially lies in its capacity to capture CO_2 from various sources (e.g., coal-based thermal power plants, cement kilns, and industrial facilities) using a variety of technologies including adsorption, chemical looping, membrane gas separation, or gas hydration (Al-Khdheeawi et al., 2023; Iglauer, 2017; Wu et al., 2022). The captured CO_2 is securely transported to the site where it can be injected into the underground porous media for long-term storage. The underground geological storage site commonly used for CO_2 geosequestration includes deep saline aquifers (Bachu, 2015; Glubokovskikh et al., 2020), depleted oil and gas reservoirs (Paluszny et al., 2020), unmineable coal seams (Kuang et al., 2023; Li et al., 2022; Zheng et al., 2020), basaltic rocks (Iglauer et al., 2020; Iglauer and Al-Yaseri, 2021), and one of the most important and advanced ones are shale formations. Apart from CO_2 geosequestration, CO_2 injection into shale formations also assists in achieving enhanced oil recovery (EOR) or enhanced gas recovery (EGR) effectively. With the depletion of conventional oil and gas reserves, EOR and EGR techniques have gained significant attention in unconventional shale formations (Dong et al., 2022; Gong et al., 2022). Laboratory and pilot tests haves identified CO_2 injection as an effective approach to strongly improve hydrocarbon recovery, particularly in mobilizing residual oil and gas that is adsorbed on OM within shale nanopore structure (Zhu et al., 2019).

Such EOR/EGR projects can be carried out at a laboratory scale using a core flooding system for CO_2 injection. This is commonly achieved in EOR/EGR using one fluid (e.g., CO_2) to displace other fluids (e.g., gas, oil) residing in the pore structure of a rock (Rezaee and Ekundayo, 2022). By combining standard core flooding and NMR experiments, the dynamic fluid flow through the shale can be observed (Fig. 11). Once CO_2 has been injected into the nanopore structure of a shale, competitive adsorption of CO_2 versus hydrocarbon mixtures (e.g., C_1/CO_2, nC_4/CO_2, and C_1/nC_4) occurs (Zhou et al., 2018). Molecular simulations revealed that CO_2 adsorbs more strongly on OM pore surfaces than C_1 or lighter components (Zhou et al., 2019). However, CO_2 is less effective in replacing nC_4 and heavier hydrocarbon components, as the affinity between OM and alkane increases with carbon chain length (Liu et al., 2019d; Zhu et al., 2019). Moreover, pore sizes largely influence the efficiency of CO_2-EOR in shale – indeed hydrocarbons in larger pores are more easily recovered than those in smaller pores. Considering that shales contain hydrocarbons mostly in smaller pores, it is important to identify strategies to enhance hydrocarbon recovery from smaller pores. Additionally, CO_2-EOR efficiency is also affected by the CO_2 injection scheme (e.g., H_2O–alternating-CO_2 (CO_2-WAG), immiscible CO_2 flooding, miscible CO_2 flooding, and CO_2 huff-n-puff (cyclic CO_2 injection)) (Xiao et al., 2017) – importantly, the recovery efficiency of different injection schemes depends strongly on sample permeability. Moreover, caused by the nanometer-scale pore structure, shales have exclusive flow behavior. This is due to the nanopore confinement effect which influences phase equilibria and reduces CO_2-oil interfacial tension which again leads to a reduced minimum miscibility pressure (MMP) of CO_2 - thus miscible conditions can be more readily achieved (Zhang et al., 2016). The miscible CO_2 flooding (injection pressure > MMP) has a higher efficiency than immiscible CO_2 flooding (injection pressure < MMP) due to the reduction of viscosity. Furthermore, NMR can also be applied in monitoring the migration and distribution of nanofluids in the complex pore structures during the EOR process. It is revealed that the EOR potential of the different nanofluids follows the order: anionic-nonionic > anionic > nonionic > amphoteric > cationic > brine (Zhang et al., 2022).

What is worth mentioning, typical NMR core flooding apparatus (used in CCUS) includes low-field and high-field NMR core flooding systems. The high-field NMR core flooding apparatus used in Berea sandstone or glass bead packs of higher porosity and permeability is not well adaptable for shales, as shales generally contain a high content of paramagnetic minerals that impact the performance of high-field NMR (Xu et al., 2019). In contrast, the low-field NMR core flooding apparatus

Table 5
Wettabilities measured for various shales.

Shale Formation	Wettability	Method	Reference
Barnett (US)	mixed wettability	WI calculated by Eq. 3.6.3 using imbibition of oil and water, coupled with contact angle measurement	(Ozen, 2011; Odusina and Sigal, 2011)
Devonian-Mississippian (US)	water-wet	WI calculated by Eq. 3.6.3 using imbibition of oil and water	Gupta et al. (2019a)
Duvernay	larger pores are more water-wet, smaller pores more oil-wet	Imbibition of oil and water experiments	Yassin et al. (2017)
Eagle Ford (US)	mixed wettability	WI calculated by Eq. 3.6.3 using imbibition of oil and water	Gupta et al. (2019a)
Eagle Ford (US)	water-wet in smaller pores, and mixed-wet in larger pores	fluid injection	Zhang et al. (2014)
Mancos (US)	water-wet in smaller pores, and mixed-wet in larger pores	fluid injection	Zhang et al. (2014)
Green River outcrop	mixed wettability to oil-wet	WI calculated by Eq. 3.6.3 using imbibition of oil and water	Gupta et al. (2019a)
Marcellus (US)	water-wet	WI calculated by Eq. 3.6.2 using imbibition of oil and water	Gupta et al. (2019b)
Marcellus (US)	mixed wettability in the small pores <60 nm	fluid injection	Zhang et al. (2014)
Wolfcamp (US)	mixed wettability	WI calculated by Eq. 3.6.2 using imbibition of oil and water	Gupta et al. (2019b)
Woodford (US)	mixed wettability to oil-wet		
Woodford (US)	mixed wettability t to oil-wet	Contact angle measurement	Kibria et al. (2018)
Upper Jurassic Haynesville (US)	–	Contact angle measurement	Kibria (2019)
Montney	water-wet	Imbibition of oil and water experiments	Lan et al. (2015)
Horn River	oil-wet		
Longmaxi (China)	mixed wettability, and stronger tendency of oil-wet	The empirical equation between contact angle and geometric mean of NMR T2 spectrum	Wang et al. (2017)
Illitic & smectitic shale	more hydrophilic	NMR T2 spectrum coupled with the spontaneous and forced imbibition	Borysenko et al. (2009)
Kaolinitic shales	potentially hydrophobic, being wet preferentially by oil and retaining that tendency after hydration.		

Note: WI from 0 to 1 is water-wet here, and WI between −1 and 0 is oil-wet. WI = 0 represents intermediate or neutral wettability. WI between −0.5 and 0.5 represents mixed wettability. Fractional wettability may also be obtained when large heterogeneity occurs in a scattered area (Looyestijn and Hofman, 2006).

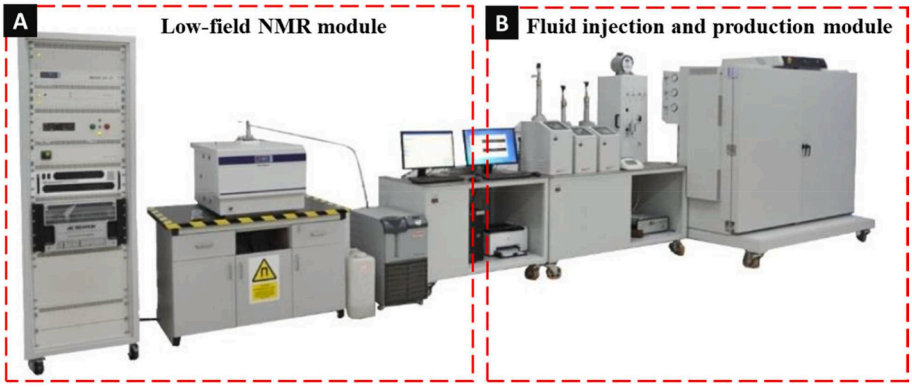

Fig. 11. NMR core flooding system (GeoSpec-2 from OXFORD) that can run experiment at reservoir pressure and temperature. (A) a low-field NMR module, (B) a fluid injection module with dual cylinder injection ISCO pumps (Source of Edith Cowan University).

consisting of a low-field NMR module and a fluid injection module works effectively in shale cases (Fig. 11).

3.9. Monitoring of gas hydrate formation and dissociation in shale

Natural gas hydrates are non-stoichiometric crystalline solids that are formed under high-pressure and low-temperature (e.g., 3–10 MPa and 275–285 K for CH_4 gas hydrate). In gas hydrates, the guest molecules (gas molecules) are trapped in water molecule cages (Klauda and Sandler, 2005; Sloan, 2003). The cages can contain light hydrocarbon and non-hydrocarbon molecules, among which methane is common (Ersland et al., 2010; Ji et al., 2019). NMR is an effective approach to discriminate and quantify the methane gas hydrate saturation and observe the formation and dissociation of methane gas hydrate from the perspective of macroscopic and microscopic scale (Bauer et al., 2015; Ge et al., 2018). Note that NMR can detect the hydrogen of a liquid phase in pore fluids, while solid hydrate is undetectable (Liu et al., 2022). Therefore, NMR T2 spectra enable real-time monitoring of the kinetic gas hydrate behavior. As gas hydrate forms, the T2 integral reduces and moves towards the faster relaxation domain; in contrast, when gas hydrate dissociates, the T2 integral increases and moves towards the slower relaxation domains (Ge et al., 2018). Gas hydrate preferentially forms in larger pores and dissociates easily in high-porosity shales with macropore sizes (Xie et al., 2022).

3.10 Underground hydrogen storage (UHS) in shale formation

To achieve a large-scale and long-term green energy storage target, underground hydrogen storage (UHS) has been proposed to be conducted in subsurface geological formations such as bedded salt caverns (Lankof and Tarkowski, 2020; Liu et al., 2020; Ozarslan, 2012), depleted oil and gas reservoirs (Amid et al., 2016; Hemme and Berk, 2018), and deep saline aquifers (Pan et al., 2021; Sainz-Garcia et al., 2017). UHS in shale formations will be an advancing and promising practice to achieve the target of green energy storage and net-zero carbon emmission.

Shale formations are characterized by fine-grained, sedimentary rock with low permeability, thus provide porous media for geological storage in UHS. Meanwhile, the petrophysical and geomechanical properties of shale as caprocks enable a good sealing integrity for long-term UHS (e.g., weak interactions are demonstrated between hydrogen and calcite-rich shale such as EagleFord and Wolfcamp shales) (Al-Yaseri et al., 2023). Furthermore, shale particles such as organic matter and clay minerals provide large specific surface areas for hydrogen adsorption (Wolff-Boenisch et al., 2023; Yuan et al., 2019). Therefore, shales perform to be a good candidate in UHS practice, while it is significant to estimate its mineralogical, geochemical, petrophysical, geomechanical and lithofacies properties, coupled with the H_2 adsorption behavior on the surface of various shale particles.

Given that NMR facility enables the detection of hydrogen, the laboratory's low-field NMR thus can be effectively applied to further investigate the injected hydrogen behaviours in UHS project in shale formations. For example, the competitive adsorption and desorption of H_2/CH_4 in kerogen or clay minerals can be further studied by integrating NMR with molecular simulation (Ho et al., 2023). Previous studies predicted that H_2 injection enables the desorption of approximately 30 % residual methane in a depleted shale gas reservoir with low gas pressure, although the interaction between CH_4 and kerogen is stronger than that between H_2 and kerogen. Meanwhile, H_2 diffusion coefficient in kerogen is predicted to be one order of magnitude higher than that of CH_4 and CO_2 (Ho et al., 2023). To fully understand the dynamic behavior of shale gas reservoir upon H_2 injection, further studies of H_2 and CH_4 adsorption/desorption behaviors on the surface of clay minerals (such as smectite, illite, chloride and kaolinite) are highly required to be conducted for large-scale UHS practices.

4. Conclusion and future outlook

NMR has been developed into a key technique in a large range of disciplines, such as physics (Bloch, 1946; Purcell et al., 1946), medical science (Dixon and Ekstrand, 1982), material science (Smith and Strange, 1996), chemistry (Claridge, 2016), food science (Alberti et al., 2002), oil & gas industry (Yuan et al., 2018b), and the state-of-art sustainable and green energy storage (e.g., CCUS (Hadian and Rezaee, 2020; Jiang et al., 2016) and UHS (Aslannezhad et al., 2023; Mahdi et al., 2021)). In the context of subsurface engineering, NMR well logging and laboratory NMR core analysis enable a comprehensive understanding of the static and dynamic behavior of the underground rock and the fluids contained in it. In unconventional shale studies, NMR has many advantages and can detect fast-relaxing fluids such as CBW and various forms of hydrocarbons (e.g., gas in mineral pores, gas in organic pores, movable oil in mineral pores, immovable oil in organic pores, and oil in mineral pores). Thus the measurement of (i) total and effective porosity, (ii) PSD and surface relaxivity, (iii) T_2 cutoff for CBW and CHW, (iv) quantification of CBW, (v) estimation of absolute permeability, (vi) fluid typing, (vii) quantification of wettability, (viii) calculation of fractal dimension are all possible. Additionally, NMR can observe the interaction between rock and various fluids during CO_2 injection during dynamic core flooding experiments (e.g. for EOR/EGR, UHS, or CCUS), and detect gas hydrate formation and dissociation in shale.

NMR also shows advantages in oil shale studies. Oil shale, unlike gas shale, is characterized by a high content of combustible organic matter, which can be converted to oil by thermal degradation (Külaots et al., 2010). As a part of OM in oil shale, kerogen is originally the solid and insoluble component with unrecoverable properties. However, kerogen can be converted into liquid shale oil and gas using retorting (pyrolysis) technology (Opik et al., 2001). NMR, bearing the advantage of multi-dimensional detection and the discrimination of various fluids, is

capable of in-situ probing the dynamics and wettability of different fluids (e.g., light and heavy hydrocarbon, water) that reside within the complex structure of shales (Korb et al., 2014). Additionally, NMR enables the real-time detection of the impact of heating rates on the conversion process of different OM components (Burnham and Singleton, 1983). Therefore, the application of NMR during oil shale in-situ conversion enables researchers to monitor the properties of kerogen and pyrolysis residues (Kang et al., 2020).

A promising future also emphasizes the combination of NMR with other techniques. For example, NMR experiment can be applied in couple with machine learning to effectively predict shale properties (Rezaee, 2022). NMR experiment can also be integrated with molecular simulation to investigate competitive gas adsorption/desorption bahavoirs. However, an open question remains in how to effectively upscale from the laboratory results and directly apply those results into a reservoir-scaled application. These knowledge gaps are highly required to be fulfilled in future studies.

Declaration of competing interest

The authors declare that they have no known competing financial interests or personal relationships that could have appeared to influence the work reported in this paper.

Data availability

The data that has been used is confidential.

Acknowledgments

Y.Y would like to acknowledge the funding of the National Natural Science Foundation of China (No. 42302162), and the Natural Science Foundation of Yunnan Province (No. 202201AU070041). Gratitudes are also expressed for Unconventional Gas Research Group at the discipline of Petroleum Engineering, WA School of Mines (WASM), Curtin University, for NMR facility assistance. Also, the authors sincerely thank the Department of Mines, Industry Regulation and Safety, the Government of Western Australia for granting us the samples under the approval of Nos. G32825 & N00413.

Appendix

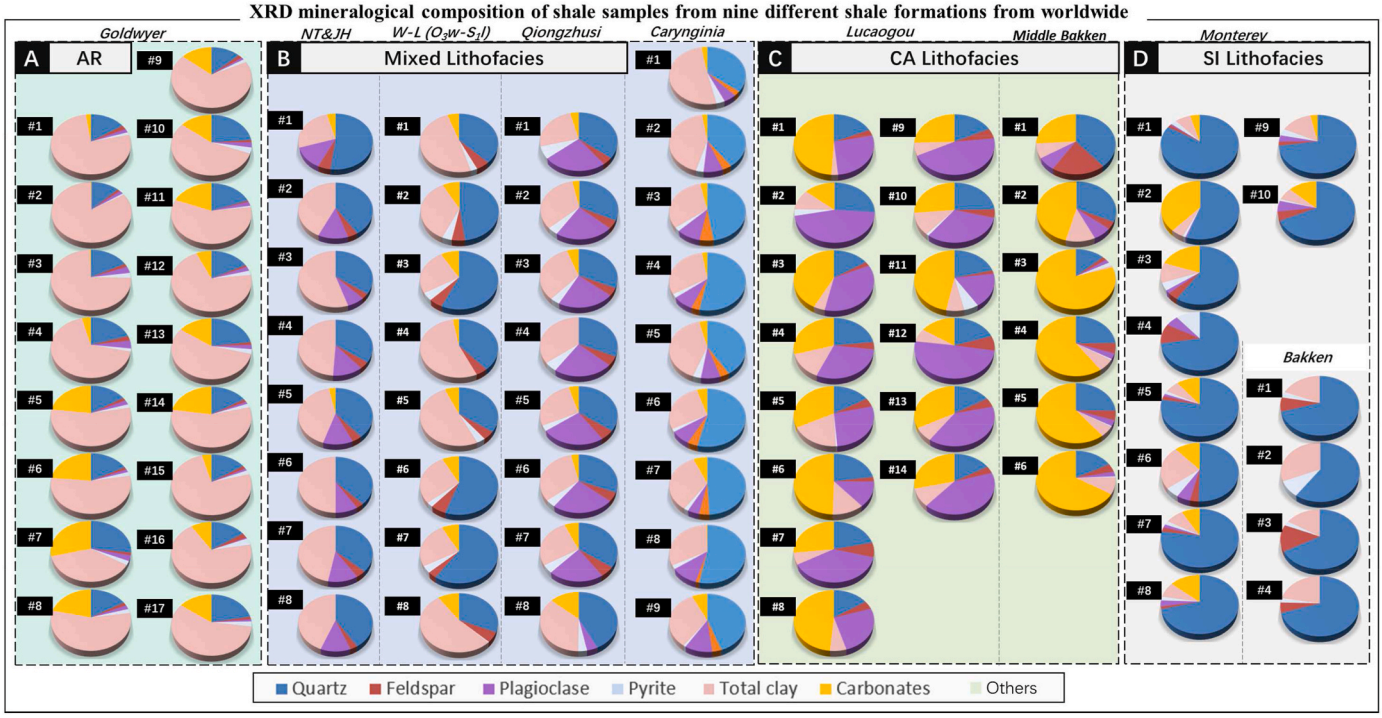

Fig. A1. XRD mineralogical composition of shale samples from various formations. The lithofacies of the studied shale samples include (i) CA lithofacies- Middle Bakken Fm. Shales (Karimi, 2017), Lucaogou Fm. Shales (Zhao et al., 2017); (ii) SI lithofacies- Monterey shale (Rivera, 2014), and Bakken shale (Yuan et al., 2021a); (iii) Mixed lithofacies: Qiongzhusi Fm. Shales (Li et al., 2017), Carynginia, Wufeng-Longmaxi (O_3w-S_1l) Fm. Shales (Zheng et al., 2019b), Ningtiaota (NT) and Jiahe (JH) (Zhang et al., 2018); and (iv) AR lithofacies- Goldwyer shales (Yuan et al., 2021a).

References

Al Hinai, A.S.H., 2014. Investigation of Gas Shale Pore Structure and its Influence on Transport Properties. Curtin University.
Alberti, E., Belton, P., Gil, A., 2002. Applications of NMR to Food Science.
Al-Yaseri, A., Amao, A., Fatah, A., 2023. Experimental investigation of shale/hydrogen geochemical interactions. Fuel 346, 128272.
Amid, A., Mignard, D., Wilkinson, M., 2016. Seasonal storage of hydrogen in a depleted natural gas reservoir. International Journal of Hydrogen Energy 41, 5549–5558.
Anderson, W., 1986. Wettability literature survey-part 2: wettability measurement. J. Petrol. Technol. 38, 1246–1262.
Arif, M., Mahmoud, M., Zhang, Y., Iglauer, S., 2021. X-ray tomography imaging of shale microstructures: a review in the context of multiscale correlative imaging. Int. J. Coal Geol. 233, 103641.
Aslannezhad, M., Ali, M., Kalantariasl, A., Sayyafzadeh, M., You, z., Iglauer, S., Keshavarz, A., 2023. A review of hydrogen/rock/brine interaction: Implications for Hydrogen Geo-storage. Progress in Energy and Combustion Science 95, 101066.

Ausbrooks, R., Hurley, N.F., May, A., Neese, D.G., 1999. Pore-size Distributions in Vuggy Carbonates from Core Images, NMR, and Capillary Pressure: SPE Annual Technical Conference and Exhibition.
Avnir, D., Farin, D., Pfeifer, P., 1984. Molecular fractal surfaces. Nature 308, 261.
Avnir, D., Jaroniec, M., 1989. An isotherm equation for adsorption on fractal surfaces of heterogeneous porous materials. Langmuir 5, 1431–1433.
Bachu, S., 2015. Review of CO2 storage efficiency in deep saline aquifers. International Journal of Greenhouse Gas Control 40, 188–202.
Bauer, K., Kulenkampff, J., Henninges, J., Spangenberg, E., 2015. Lithological control on gas hydrate saturation as revealed by signal classification of NMR logging data. J. Geophys. Res. Solid Earth 120, 6001–6017.
Bhatt, A., Helle, H.B., 2002. Committee neural networks for porosity and permeability prediction from well logs. Geophys. Prospect. 50, 645–660.
Bloch, F., 1946. Nuclear induction: Phys. Rev. 70, 460.
Borgia, G., Brown, R., Fantazzini, P., 1998. Uniform-penalty inversion of multiexponential decay data. J. Magn. Reson. 132, 65–77.
Borysenko, A., Clennell, B., Sedev, R., Burgar, I., Ralston, J., Raven, M., Dewhurst, D., Liu, K., 2009. Experimental investigations of the wettability of clays and shales. J. Geophys. Res. Solid Earth 114.
Brown, R.J., Fatt, I., 1956. Measurements of Fractional Wettability of Oil Fields' Rocks by the Nuclear Magnetic Relaxation Method: Fall Meeting of the Petroleum Branch of AIME.
Bu, H., Ju, Y., Tan, J., Wang, G., Li, X., 2015. Fractal characteristics of pores in non-marine shales from the Huainan coalfield, eastern China. J. Nat. Gas Sci. Eng. 24, 166–177.
Burnham, A.K., Singleton, M.F., 1983. High-pressure Pyrolysis of Green River Oil Shale. ACS Publications.
Bustin, A.M., Bustin, R.M., Cui, X., 2008a. Importance of Fabric on the Production of Gas Shales: SPE Unconventional Reservoirs Conference.
Bustin, R.M., Bustin, A.M., Cui, A., Ross, D., Pathi, V.M., 2008b. Impact of Shale Properties on Pore Structure and Storage Characteristics: SPE Shale Gas Production Conference.
Butler, J., Reeds, J., Dawson, S., 1981. Estimating solutions of first kind integral equations with nonnegative constraints and optimal smoothing. SIAM J. Numer. Anal. 18, 381–397.
Cao, J., Yang, R., Hu, G., Yao, S., Xie, X., Gao, Y., Gao, J., 2018. Hydrocarbon potential of the lower cretaceous mudstones in coastal southeastern China. Am. Assoc. Pet. Geol. Bull. 102, 333–366.
Carr, H.Y., Purcell, E.M., 1954. Effects of diffusion on free precession in. Nuclear Magnetic Resonance Experiments: Phys. Rev. 94, 630–638.
Chang, D., Vinegar, H.J., Morriss, C., Straley, C., 1994. Effective Porosity, Producible Fluid and Permeability in Carbonates from NMR Logging: SPWLA 35th Annual Logging Symposium.
Chen, J., Hirasaki, G., Flaum, M., 2006. NMR wettability indices: effect of OBM on wettability and NMR responses. J. Petrol. Sci. Eng. 52, 161–171.
Chen, S., Yu, H., Lu, M., Lebedev, M., Li, X., Yang, Z., Cheng, W., Yuan, Y., Ding, S., Johnson, L., 2022. A new approach to calculate gas saturation in shale reservoirs. Energy Fuels 36 (4), 1904–1915.
Claridge, T.D., 2016. High-resolution NMR Techniques in Organic Chemistry, vol. 27. Elsevier.
Coates, G.R., Galford, J., Mardon, D., Marschall, D., 1998. A New Characterization of Bulk-Volume Irreducible Using Magnetic Resonance: the Log Analyst, vol. 39.
Coates, G.R., Miller, M., Gillen, M., Henderson, C., 1991. The MRIL in Conoco 33-1 an Investigation of a New Magnetic Resonance Imaging Log: SPWLA 32nd Annual Logging Symposium.
Coates, G.R., Xiao, L., Prammer, M.G., 1999. NMR Logging: Principles and Applications. Gulf Professional Publishing.
Dixon, R.L., Ekstrand, K.E., 1982. The physics of proton NMR: Med. Phys. 9, 807–818.
Dong, M., Gong, H., Sang, Q., Zhao, X., Zhu, C., 2022. Review of CO2-kerogen interaction and its effects on enhanced oil recovery and carbon sequestration in shale oil reservoirs. Resources Chemicals and Materials 1, 93–113.
Dong, D., Shi, Z., Guang, Q., Jiang, S., Zhang, M., Zhang, C., Wang, S., Sun, S., Yu, R., Liu, D., Peng, P., Wang, S., 2018. Progress, challenges and prospects of shale gas exploration in the Wufeng-Longmaxi reservoirs in the Sichuan Basin. Nat. Gas. Ind. 38, 67–76.
Dunn, K.-J., Bergman, D.J., LaTorraca, G.A., 2002. Nuclear Magnetic Resonance: Petrophysical and Logging Applications, vol. 32. Elsevier.
Dutilleul, J., Bourlange, S., Géraud, Y., Stemmelen, D., 2020. Porosity, pore structure, and fluid distribution in the sediments entering the northern hikurangi margin, New Zealand. J. Geophys. Res. Solid Earth 125 e2020JB020330.
Easley, T.G., Sigal, R., Rai, C., 2007. Thermogravimetric Analysis of Barnett Shale Samples: Society of Core Analysts Annual Symposium. Canada, Calgary, Alberta.
Ersland, G., Huseb, J., Graue, A., Baldwin, B.A., Howard, J., Stevens, J., 2010. Measuring gas hydrate formation and exchange with CO2 in Bentheim sandstone using MRI tomography. Chem. Eng. J. 158, 25–31.
Eslinger, E., Pevear, D.R., 1988. Clay Minerals for Petroleum Geologists and Engineers. Society of Economic Paleontologists and Mineralogis ts.
Fleury, M., 2007. NMR surface relaxivity determination using NMR apparent diffusion curves and BET measurements. In: International Symposium of the Society of Core Analysts, pp. 10–12.
Fleury, M., Deflandre, F., 2003. Quantitative evaluation of porous media wettability using NMR relaxometry. Magn. Reson. Imaging 21, 385–387.
Fleury, M., Romero-Sarmiento, M., 2016. Characterization of shales using T1–T2 NMR maps. J. Petrol. Sci. Eng. 137, 55–62.
Folk, R.L., 1980. Petrology of Sedimentary Rocks. Hemphill Publishing Company.
Freedman, R., 2006. Advances in NMR logging. J. Petrol. Technol. 58, 60–66.
Freedman, R., Johnston, M., Morriss, C., Straley, C., Tutunjian, P., Vinegar, H., 1997. Hydrocarbon saturation and viscosity estimation from NMR logging in the Belridge Diatomite. Log. Anal. 38.
Furmann, A., Mastalerz, M., Bish, D., Schimmelmann, A., Pedersen, P.K., 2016. Porosity and pore size distribution in mudrocks from the belle fourche and second white specks formations in alberta, Canada. AAPG (Am. Assoc. Pet. Geol.) Bull. 100, 1265–1288.
Gao, H., Li, H.A., 2016. Pore structure characterization, permeability evaluation and enhanced gas recovery techniques of tight gas sandstones. J. Nat. Gas Sci. Eng. 28, 536–547.
Ge, X., Liu, J., Fan, Y., Xing, D., Deng, S., Cai, J., 2018. Laboratory investigation into the formation and dissociation process of gas hydrate by low-field NMR technique. J. Geophys. Res. Solid Earth 123, 3339–3346.
Ge, X., Myers, M.T., Liu, J., Fan, Y., Zahid, M.A., Zhao, J., Hathon, L.J.M., Geology, P., 2021. Determining the Transverse Surface Relaxivity of Reservoir Rocks: A Critical Review and Perspective, 104934.
Glubokovskikh, S., Pevzner, R., Gunning, J., Dance, T., Shulakova, V., Popik, D., Popik, S., Bagheri, M., Gurevich, B., 2020. How well can time-lapse seismic characterize a small CO2 leakage into a saline aquifer: CO2CRC Otway 2C experiment (Victoria, Australia). International Journal of Greenhouse Gas Control 92, 102854.
Golub, G.H., Heath, M., Wahba, G., 1979. Generalized cross-validation as a method for choosing a good ridge parameter. Technometrics 21, 215–223.
Gong, H., Zhang, H., Lv, W., Xu, L., Li, Z., Dong, M., 2022. Effects of Kerogen on the flow and EOR performance of oil in shale cores during CO2 flooding process investigated by NMR technology. SPE Journal 27, 2244–2256.
Guo, Y., Li, X., Huang, L., 2022. Insight into spontaneous water-based working fluid imbibition on the dynamic tensile behavior of anisotropic shale. Eng. Geol. 308, 106830.
Gupta, I., Rai, C., Sondergeld, C., 2019a. Study impact of sample treatment and insitu fluids on shale wettability measurement using NMR. J. Petrol. Sci. Eng. 176, 352–361.
Gupta, I., Rai, C., Sondergeld, C., Hofmann, R., 2019b. Water Weakening: A Laboratory Study of Marcellus, Woodford, Eagle Ford, and Wolfcamp Shales. SPE Reservoir Evaluation & Engineering.
Hadian, P., Rezaee, R., 2020. The effect of supercritical CO2 on. Shaly Caprocks: Energies 13, 149.
Hao, F., Zou, H., Lu, Y., 2013. Mechanisms of shale gas storage: implications for shale gas exploration in China. AAPG Bull. 97, 1325–1346.
Hemme, C., Berk, W.V., 2018. Hydrogeochemical Modeling to Identify Potential Risks of Underground Hydrogen Storage in Depleted Gas Fields. Applied Sciences 8, 2282.
Ho, T.A., Dang, S.T., Dasgupta, N., Choudhary, A., Rai, C.S., Wang, Y., 2023. Nuclear magnetic resonance and molecular simulation study of H2 and CH4 adsorption onto shale and sandstone for hydrogen geological storage. International Journal of Hydrogen Energy.
Hu, Q., Ewing, R.P., Rowe, H.D., 2015. Low nanopore connectivity limits gas production in Barnett formation. J. Geophys. Res. Solid Earth. 120, 8073–8087.
Hurlimann, M., Helmer, K.G., Latour, L., Sotak, C.H., 1994. Restricted diffusion in sedimentary rocks. Determination of surface-area-to-volume ratio and surface relaxivity. J. Magn. Reson., Ser. A 111, 169–178.
Iglauer, S., 2017. CO2–water–rock wettability: variability, influencing factors, and implications for CO2 geostorage. Accounts Chem. Res. 50, 1134–1142.
Iglauer, S., Al-Yaseri, A., 2021. Improving basalt wettability to de-risk CO2 geo-storage in basaltic formations. Advances in Geo-Energy Research 5, 347–350.
Iglauer, S., Al-Yaseri, A.Z., Wolff-Boenisch, D., 2020. Basalt-CO2-brine wettability at storage conditions in basaltic formations. International Journal of Greenhouse Gas Control 102, 103148.
Iglauer, S., Fernø, M., Shearing, P., Blunt, M., 2012. Comparison of residual oil cluster size distribution, morphology and saturation in oil-wet and water-wet sandstone. J. Colloid Interface Sci. 375, 187–192.
Javadpour, F., 2009. Nanopores and apparent permeability of gas flow in mudrocks (shales and siltstone). J. Can. Petrol. Technol. 48, 16–21.
Ji, Y., Hou, J., Cui, G., Lu, N., Zhao, E., Liu, Y., Du, Q., 2019. Experimental study on methane hydrate formation in a partially saturated sandstone using low-field NMR technique. Fuel 251, 82–90.
Jiang, Y., Luo, Y., Lu, Y., Qin, C., Liu, H., 2016. Effects of supercritical CO_2 treatment time, pressure, and temperature on microstructure of shale. Energy 97, 173–181.
Jin, Z., 2023. Hydrocarbon accumulation and resources evaluation: Recent advances and current challenges. Advances in Geo-Energy Research 8 (1), 1–4.
Jin, Z., Zhang, J., Tang, X., 2022. Unconventional natural gas accumulation system. Nat. Gas. Ind. B 9, 9–19.
Külaots, I., Goldfarb, J.L., Suuberg, E.M., 2010. Characterization of Chinese, American and Estonian oil shale semicokes and their sorptive potential. Fuel 89, 3300–3306.
Kadkhodaie-Ilkhchi, A., Rahimpour-Bonab, H., Rezaee, M., 2009. A committee machine with intelligent systems for estimation of total organic carbon content from petrophysical data: an example from Kangan and Dalan reservoirs in South Pars Gas Field. Iran: Comput. Geosci. 35, 459–474.
Kang, Z., Zhao, Y., Yang, D., 2020. Review of oil shale in-situ conversion technology. Appl. Energy 269, 115121.
Karimi, S., 2017. Pore-Scale Assessment of Middle Bakken Reservoir Using Centrifuge, Mercury Injection, Nitrogen Adsorption, NMR, and Resistivity Instruments. Colorado School of Mines.
Katz, A., Thompson, A., 1985. Fractal sandstone pores: implications for conductivity and pore formation. Phys. Rev. Lett. 54, 1325.
Kausik, R., Fellah, K., Feng, L., Simpson, G., 2017. High-and low-field NMR relaxometry and diffusometry of the bakken petroleum system. Petrophysics 58, 341–351.

Kausik, R., Fellah, K., Rylander, E., Singer, P.M., Lewis, R.E., Sinclair, S.M., 2016. NMR relaxometry in shale and implications for logging. Petrophysics 57, 339–350.
Keating, K., Knight, R., 2010. A laboratory study of the effect of Fe (II)-bearing minerals on nuclear magnetic resonance (NMR) relaxation measurements. Geophysics 75, F71–F82.
Keating, K., Knight, R., 2012. The effect of spatial variation in surface relaxivity on nuclear magnetic resonance relaxation ratesSpatially variable surface relaxivity. Geophysics 77, E365–E377.
Kenyon, B., Kleinberg, R., Straley, C., Gubelin, G., Morriss, C., 1995. Nuclear magnetic resonance imaging—technology for the 21st century. Oilfield Rev. 7, 19–33.
Kenyon, W., 1992. Nuclear magnetic resonance as a petrophysical measurement: the International journal of radiation applications and instrumentation. Part E. Nuclear geophysics 6, 153–171.
Kenyon, W., Day, P., Straley, C., Willemsen, J., 1988. A three-part study of NMR longitudinal relaxation properties of water-saturated sandstones. SPE Form. Eval. 3, 622–636.
Khatibi, S., Ostadhassan, M., Xie, Z.H., Gentzis, T., Bubach, B., Gan, Z., Carvajal-Ortiz, H., 2019. NMR relaxometry a new approach to detect geochemical properties of organic matter in tight shales. Fuel 235, 167–177.
Kibria, M.G., 2019. Shale Gas/Oil Reservoir Characterization and Maturity Determination Based on Various Experimental Analyses.
Kibria, M.G., Hu, Q., Liu, H., Zhang, Y., Kang, J., 2018. Pore structure, wettability, and spontaneous imbibition of Woodford shale. Permian Basin, West Texas: Mar. Petrol. Geol. 91, 735–748.
Klauda, J.B., Sandler, S.I., 2005. Global distribution of methane hydrate in ocean sediment. Energy Fuels 19, 459–470.
Kleinberg, R., 1996. Utility of NMR T2 distributions, connection with capillary pressure, clay effect, and determination of the surface relaxivity parameter ρ2. Magn. Reson. Imaging 14, 761–767.
Kolodzie, S., 1980. Analysis of Pore Throat Size and Use of the Waxman-Smits Equation to Determine OOIP in Spindle Field, Colorado: SPE Annual Technical Conference and Exhibition.
Korb, J.-P., Nicot, B., Louis-Joseph, A., Bubici, S., Ferrante, G., 2014. Dynamics and wettability of oil and water in oil shales. J. Phys. Chem. C 118, 23212–23218.
Kuang, N., Zhou, J., Xian, X., Zhang, C., Yang, K., Dong, Z., 2023. Geomechanical risk and mechanism analysis of CO2 sequestration in unconventional coal seams and shale gas reservoirs. Rock Mechanics Bulletin 2, 100079.
Kuila, U., 2013. Measurement and Interpretation of Porosity and Pore-Size Distribution in Mudrocks: the Hole Story of Shales. Colorado School of Mines. Arthur Lakes Library.
Kuila, U., Mccarty, D.K., Derkowski, A., Fischer, T.B., Prasad, M., 2014. Total porosity measurement in gas shales by the water immersion porosimetry (WIP) method. Fuel 117, 1115–1129.
Labani, M.M., Kadkhodaie-Ilkhchi, A., Salahshoor, K., 2010. Estimation of NMR log parameters from conventional well log data using a committee machine with intelligent systems: a case study from the Iranian part of the South Pars gas field. Persian Gulf Basin: J. Petrol. Sci. Eng. 72, 175–185.
Lai, J., Wang, G., Wang, Z., Chen, J., Pang, X., Wang, S., Zhou, Z., He, Z., Qin, Z., Fan, X., 2018. A review on pore structure characterization in tight sandstones. Earth Sci. Rev. 177, 436–457.
Lan, Q., Xu, M., Binazadeh, M., Dehghanpour, H., Wood, J.M., 2015. A comparative investigation of shale wettability: the significance of pore connectivity. J. Nat. Gas Sci. Eng. 27, 1174–1188.
Lankof, L., Tarkowski, R., 2020. Assessment of the potential for underground hydrogen storage in bedded salt formation. International Journal of Hydrogen Energy 45, 19479–19492.
Lawson, C.L., Hanson, R.J., 1995. Solving Least Squares Problems. SIAM.
Li, J., Cai, J., 2023. Quantitative characterization of fluid occurrence in shale reservoirs. Advances in Geo-Energy Research 9, 146–151.
Li, A., Ding, W., Wang, R., He, J., Wang, X., Sun, Y., Gu, Y., Jiao, N., 2017. Petrophysical characterization of shale reservoir based on nuclear magnetic resonance (NMR) experiment: a case study of Lower Cambrian Qiongzhusi Formation in eastern Yunnan Province, South China. J. Nat. Gas Sci. Eng. 37, 29–38.
Li, X., Yu, H., Lebedev, M., Lu, M., Yuan, Y., Yang, Z., Cheng, W., Chen, S., Zhan, J., Ding, S., Johnson, L., 2022. The influence of CO2 saturated brine on microstructure of coal: implications for carbon geo-sequestration. Front. Energy Res. 10.
Liu, B., Wang, H., Fu, X., Bai, Y., Bai, L., Jia, M., He, B., 2019a. Lithofacies and depositional setting of a highly prospective lacustrine shale oil succession from the Upper Cretaceous Qingshankou Formation in the Gulong sag, northern Songliao Basin, northeast China. AAPG (Am. Assoc. Pet. Geol.) Bull. 103, 405–432.
Liang, Y., Tan, Y., Wang, F., Luo, Y., Zhao, Z., 2020. Improving permeability of coal seams by freeze-fracturing method: The characterization of pore structure changes under low-field NMR. Energy Reports 6, 550–561.
Liu, K., Jin, Z., Zeng, L., Yuan, Y., Ostadhassan, M., 2021. Determination of Clay Bound Water in Shales from NMR Signals: the Fractal Theory. Energy & Fuels 35 (22), 18406–18413.
Liu, K., Mirzaei-Paiaman, A., Liu, B., Ostadhassan, M., 2020. A new model to estimate permeability using mercury injection capillary pressure data: application to carbonate and shale samples. J. Nat. Gas Sci. Eng. 84, 103691.
Liu, K., Ostadhassan, M., Hackley, P., Gentzis, T., Zou, J., Yuan, Y., Carvajal-Ortiz, H., Rezaee, R., Bubach, B., 2019b. Experimental study on the impact of thermal maturity on shale microstructures using hydrous pyrolysis. Energy Fuels 33, 9702–9719.
Liu, K., Ostadhassan, M., Sun, L., Zou, J., Yuan, Y., Gentzis, T., Zhang, Y., Carvajal-Ortiz, H., Rezaee, R., 2019c. A comprehensive pore structure study of the Bakken Shale with SANS, N2 adsorption and mercury intrusion. Fuel 245, 274–285.
Liu, Z., Liu, D., Cai, Y., Yao, Y., Pan, Z., Zhou, Y., 2019. Application of nuclear magnetic resonance (NMR) in coalbed methane and shale reservoirs: A review. International Journal of Coal Geology 103261.
Liu, Y., Ma, X., Li, H.A., Hou, J., 2019d. Competitive adsorption behavior of hydrocarbon (s)/CO2 mixtures in a double-nanopore system using molecular simulations. Fuel 252, 612–621.
Liu, Y., Yao, Y., Liu, D., Zheng, S., Sun, G., Chang, Y., 2018. Shale Pore Size Classification: an NMR Fluid Typing Method: Marine and Petroleum Geology.
Liu, B., Zhan, L., Lu, H., Lu, X., Cai, W., 2022. Effect of the Temperature and Tetrahydrofuran (THF) Concentration on THF Hydrate Formation in Aqueous Solution. 36 (18), 10642–10651.
Liu, W., Zhang, Z., Chen, J., Jiang, D., Wu, F., Fan, J., Li, Y., 2020. Feasibility evaluation of large-scale underground hydrogen storage in bedded salt rocks of China: A case study in Jiangsu province. Energy 198, 117348.117341–117348.117316.
Looyestijn, W.J., Hofman, J., 2006. Wettability-index determination by nuclear magnetic resonance. SPE Reservoir Eval. Eng. 9, 146–153.
Loucks, R.G., Ruppel, S.C., 2007. Mississippian Barnett shale: lithofacies and depositional setting of a deep-water shale-gas succession in the fort worth basin. Texas: AAPG Bull. 91, 579–601.
Luffel, D., Guidry, F., 1992. New core analysis methods for measuring reservoir rock properties of Devonian shale. J. Petrol. Technol. 44, 1,184-1,190.
Mahamud, M.M., Novo, M.F., 2008. The use of fractal analysis in the textural characterization of coals. Fuel 87, 222–231.
Mahdi, D.S., Al-Khdheeawi, E.A., Yuan, Y., Zhang, Y., Iglauer, S., 2021. Hydrogen underground storage efficiency in a heterogeneous sandstone reservoir. Advances in Geo-Energy Research 5, 437–443.
Malki, H.A., Baldwin, J., 2002. A neuro-fuzzy based oil/gas producibility estimation method: proceedings of the 2002 International Joint Conference on Neural Networks. IJCNN'02 (Cat. No. 02CH37290) 896–901.
Mandelbrot, B.B., Passoja, D.E., Paullay, A.J., 1984. Fractal character of fracture surfaces of metals. Nature 308, 721.
Mangi, H.N., Detian, Y., Hameed, N., Ashraf, U., Rajper, R.H., 2020. Pore structure characteristics and fractal dimension analysis of low rank coal in the Lower Indus Basin, SE Pakistan. J. Nat. Gas Sci. Eng. 77, 103231.
Mastalerz, M., He, L., Melnichenko, Y.B., Rupp, J.A., 2012. Porosity of coal and shale: insights from gas adsorption and SANS/USANS techniques. Energy Fuels 26, 5109–5120.
Mastalerz, M., Schimmelmann, A., Drobniak, A., Chen, Y., 2013. Porosity of Devonian and Mississippian New Albany Shale across a maturation gradient: insights from organic petrology, gas adsorption, and mercury intrusion. AAPG Bull. 97, 1621–1643.
Meiboom, S., Gill, D., 1958. Modified spin-echo method for measuring nuclear relaxation times. Rev. Sci. Instrum. 29, 688–691.
Ngo, V.T., Lu, V.D., Le, V.M., 2018. A comparison of permeability prediction methods using core analysis data for sandstone and carbonate reservoirs. Geomechanics and Geophysics for Geo-Energy and Geo-Resources 4, 129–139.
Ngo, V.T., Lu, V.D., Nguyen, M.H., Hoang, T.M., Nguyen, H.M., Le, V.M., 2015. A Comparison of Permeability Prediction Methods Using Core Analysis Data: SPE Reservoir Characterisation and Simulation Conference and Exhibition.
Odusina, E., Sigal, R.F., 2011. Laboratory NMR measurements on methane saturated Barnett Shale samples. Petrophysics 52, 32–49.
Odusina, E.O., Sondergeld, C.H., Rai, C.S., 2011. NMR Study of Shale Wettability: Canadian Unconventional Resources Conference.
Ogilvie, S., Cuddy, S., Lindsay, C., Hurst, A., 2002. Novel Methods of Permeability Prediction from NMR Tool Data: Dialog. London Petrophysical Society, London, pp. 1–14.
Opik, I., Golubev, N., Kaidalov, A., Kann, J., Elenurm, A., 2001. Current status of oil shale processing in solid heat carrier UTT (Galoter) retorts in Estonia. Oil Shale 18, 99–107.
Ozarslan, A., 2012. Large-scale hydrogen energy storage in salt caverns. International Journal of Hydrogen Energy 37, 14265–14277.
Ozen, A.E., 2011. Comparisons of T1 and T2 NMR Relaxations on Shale Cuttings. University of Oklahoma Norman, OK.
Pan, B., Yin, X., Ju, Y., Iglauer, S., 2021. Underground hydrogen storage: Influencing parameters and future outlook. Advances in Colloid and Interface Science 102473.
Pan, B., Yin, X., Zhu, W., Yang, Y., Ju, Y., Yuan, Y., Iglauer, S., 2022. Theoretical study of brine secondary imbibition in sandstone reservoirs: implications for H2, CH4, and CO2 geo-storage. Int. J. Hydrogen Energy. 47, 18058–18066.
Paluszny, A., Graham, C.C., Daniels, K.A., Tsaparli, V., Zimmerman, R.W., 2020. Caprock integrity and public perception studies of carbon storage in depleted hydrocarbon reservoirs. International Journal of Greenhouse Gas Control 98, 103057.
Pan, Z., Ma, Y., Connell, L.D., Down, D.I., Camilleri, M., 2015. Measuring anisotropic permeability using a cubic shale sample in a triaxial cell. J. Nat. Gas Sci. Eng. 26, 336–344.
Passey, Q.R., Bohacs, K., Esch, W.L., Klimentidis, R., Sinha, S., 2010. From Oil-Prone Source Rock to Gas-Producing Shale Reservoir-Geologic and Petrophysical Characterization of Unconventional Shale Gas Reservoirs: International Oil and Gas Conference and Exhibition in China.
Pittman, E.D., 1992. Relationship of porosity and permeability to various parameters derived from mercury injection-capillary pressure curves for sandstone. AAPG Bull. 76, 191–198.
Prammer, M., Drack, E., Bouton, J., Gardner, J., 1996. Measurements of clay-bound water and total porosity by magnetic resonance logging. Log. Anal. 37.
Prammer, M., Mardon, D., Coates, G., Miller, M., 1995. In: Lithology-independent Gas Detection by Gradient-NMR Logging: SPE Annual Technical Conference and Exhibition.

Purcell, E.M., Torrey, H.C., Pound, R.V., 1946. Resonance absorption by nuclear magnetic moments in a solid. Phys. Rev. 69, 37.
Rezaee, M., Jafari, A., Kazemzadeh, E., 2006. Relationships between permeability, porosity and pore throat size in carbonate rocks using regression analysis and neural networks. J. Geophys. Eng. 3, 370–376.
Rezaee, R., 2015. Fundamentals of Gas Shale Reservoirs. John Wiley & Sons.
Rezaee, R., 2022. Synthesizing nuclear magnetic resonance (NMR) outputs for clastic rocks using machine learning methods, examples from north west shelf and perth basin, western Australia. Energies 15, 518.
Rezaee, R., Ekundayo, J., 2022. Permeability prediction using machine learning methods for the CO2 injectivity of the precipice sandstone in surat basin. Aust. Now.: Energies 15, 2053.
Rezaee, R., Saeedi, A., Clennell, B., 2012. Tight gas sands permeability estimation from mercury injection capillary pressure and nuclear magnetic resonance data. J. Petrol. Sci. Eng. 88, 92–99.
Rivera, S., 2014. Ultrasonic and Low Field Nuclear Magnetic Resonance Study of Lower Monterey Formation: San Joaquin Basin, Colorado School of Mines. Arthur Lakes Library.
Rylander, E., Singer, P., Jiang, T., Lewis, R., Sinclair, S., Mclin, R.H., 2013. NMR T_2 Distributions in the Eagle Ford Shale: Reflections on Pore Size. SPE Unconventional Resources Conference-USA.
Saidian, M., Livo, K., Prasad, M., 2015. Effect of Paramagnetic Mineral Content and Distribution on Surface Relaxivity in Organic-Rich Niobrara and Haynesville Shales. SEG Technical Program Expanded Abstracts 2015, Society of Exploration Geophysicists, pp. 2671–2676.
Saidian, M., Prasad, M., 2015. Effect of mineralogy on nuclear magnetic resonance surface relaxivity: a case study of Middle Bakken and Three Forks formations. Fuel 161, 197–206.
Sainz-Garcia, A., Abarca, E., Rubi, V., Grandia, F., 2017. Assessment of feasible strategies for seasonal underground hydrogen storage in a saline aquifer. International Journal of Hydrogen Energy 42, 16657–16666.
Shang, Z., Dong, L., Niu, L., Shi, H., 2019. Adsorption of Methane, Nitrogen, and Carbon Dioxide in Atomic-Scale Fractal Nanopores by Monte Carlo Simulation I: Single-Component Adsorption. Energy & Fuels.
Sigal, R.F., 2015. Pore-size distributions for organic-shale-reservoir rocks from nuclear-magnetic-resonance spectra combined with adsorption measurements. SPE J. 20, 824–830.
Sigal, R.F., Odusina, E., 2011. Laboratory NMR measurements on methane saturated Barnett Shale samples. Petrophysics 52, 32–49.
Singer, P.M., Chen, Z., Hirasaki, G.J., 2016. Fluid typing and pore size in organic shale using 2D NMR in saturated kerogen isolates. Petrophysics 57, 604–619.
Slijkerman, W.F., Hofman, J.P., Looyestijn, W.J., Volokitin, Y., 2001. A Practical Approach to Obtain Primary Drainage Capillary Pressure Curves from NMR Core and Log Data, vol. 42. Petrophysics.
Sloan, E.D., 2003. Fundamental principles and applications of natural gas hydrates. Nature 426, 353–359.
Smith, M.E., Strange, J.H., 1996. NMR techniques in materials physics. A review: Meas. Sci. Technol. 7, 449.
Sondergeld, C.H., Newsham, K.E., Comisky, J.T., Rice, M.C., Rai, C.S., 2010. Petrophysical Considerations in Evaluating and Producing Shale Gas Resources: SPE Unconventional Gas Conference.
Straley, C., Rossini, D., Vinegar, H., Tutunjian, P., Morriss, C., 1997. Core Analysis by Low-Field NMR, vol. 38. The Log Analyst.
Sulucarnain, I.D., Sondergeld, C.H., Rai, C.S., 2012. An NMR Study of Shale Wettability and Effective Surface Relaxivity: SPE Canadian Unconventional Resources Conference.
Sun, M., Zhao, J., Pan, Z., Hu, Q., Yu, B., Tan, Y., Sun, L., Bai, L., Wu, C., Blach, T.P., Zhang, Y., Zhang, C., Cheng, G., 2020. Pore characterization of shales: a review of small angle scattering techniqueJ. Nat. Gas Sci. Eng. 78, 103294.
Swanson, B., 1981. A simple correlation between permeabilities and mercury capillary pressures. J. Petrol. Technol. 33, 2498–2504.
Tamhane, D., Wong, P., Aminzadeh, F., Nikravesh, M., 2000. Soft Computing for Intelligent Reservoir Characterization: SPE Asia Pacific Conference on Integrated Modelling for Asset Management.
Tan, M., Mao, K., Song, X., Yang, X., Xu, J., 2015. NMR petrophysical interpretation method of gas shale based on core NMR experiment. J. Petrol. Sci. Eng. 136, 100–111.
Testamanti, M.N., 2018. Assessment of Fluid Transport Mechanisms in Shale Gas Reservoirs. Curtin University.
Testamanti, M.N., Rezaee, R., 2018. Considerations for the acquisition and inversion of NMR T2 data in shales. J. Petrol. Sci. 174, 177–188.
Testamanti, M.N., Rezaee, R., Yuan, Y., Pan, D., 2017. Determination of T2 cut-off for shale reservoirs: a case study from the Caryginia formation, Perth Basin, Western Australia. The APPEA Journal 57, 664–668.
Tian, H., Li, H., Zhang, T., Xiao, X., 2016. Characterization of methane adsorption on overmature Lower Silurian–Upper Ordovician shales in Sichuan Basin, southwest China: Experimental results and geological implications. International Journal of Coal Geology 156, 36–49.
Tian, H., Pan, L., Xiao, X.M., Wilkins, R.W.T., Meng, Z.P., Huang, B.J., 2013. A preliminary study on the pore characterization of Lower Silurian black shales in the Chuandong Thrust Fold Belt, Southwestern China using low pressure N2 adsorption and FE-SEM methodsMar. Pet. Geol. 48, 8–19.
Tian, H., Pan, L., Zhang, T., Xiao, X., Meng, Z., Huang, B., 2015. Pore characterization of organic-rich Lower Cambrian shales in Qiannan Depression of Guizhou Province, Southwestern China. Mar. Pet. Geol. 62, 28–43.
Topór, T., Derkowski, A., Kuila, U., Fischer, T.B., McCarty, D.K., 2016. Dual liquid porosimetry: a porosity measurement technique for oil-and gas-bearing shales. Fuel 183, 537–549.
Valori, A., Nicot, B., 2019. A review of 60 years of NMR wettability. Petrophysics 60, 255–263.
Wang, L., Fu, Y., Li, J., Sima, L., Wu, Q., Jin, W., Wang, T., 2017. Experimental study on the wettability of Longmaxi gas shale from Jiaoshiba gas field, Sichuan Basin, China. J. Petrol. Sci. Eng. 151, 488–495.
Wolff-Boenisch, D., Abid, H.R., Tucek, J.E., Keshavarz, A., Iglauer, S., 2023. Importance of clay-H2 interactions for large-scale underground hydrogen storage. International journal of hydrogen energy.
Wu, S., Yu, C., Hu, X., et al., 2022. Characterization of mineral and pore evolution under CO2-brine-rock interaction at in-situ conditions. Advances in Geo-Energy Research 6 (2), 177–178.
Wu, S., Zhu, R., Cui, J., Cui, J., Bai, B., Zhang, X., Jin, X., Zhu, D., You, J., Li, X., 2015. Characteristics of lacustrine shale porosity evolution, Triassic Chang 7 member, Ordos Basin, NW China. Petrol. Explor. Dev. 42, 185–195.
Xiao, L., Li, J., Mao, Z., Lu, J., Yu, H., Guo, H., Li, G., 2018. A method to determine nuclear magnetic resonance (NMR) T 2 cutoff based on normal distribution simulation in tight sandstone reservoirs. Fuel 225, 472–482.
Xiao, L., Wang, H., Zou, C.-c., Mao, Z.-q., Guo, H.-p., 2016. Improvements on "Application of NMR logs in tight gas reservoirs for formation evaluation: a case study of Sichuan basin in China". J. Petrol. Sci. Eng. 138, 11–17.
Xiao, X.M., Wei, Q., Gai, H.F., Li, T.F., Wang, M.L., Pan, L., Chen, J., Tian, H., 2015. Main controlling factors and enrichment area evaluation of shale gas of the lower paleozoic marine strata in South China. Petrol. Sci. 12, 573–586.
Xiao, P., Yang, Z., Wang, X., Xiao, H., Wang, X., 2017. Experimental investigation on CO2 injection in the Daqing extra/ultra-low permeability reservoir. J. Petrol. Sci. Eng. 149, 765–771.
Xie, Y., Cai, H., Deng, W., Kuang, Z., Wang, T., Kang, D., Zhu, C., 2022. The in-situ NMR evidence of gas hydrate forming in micro-pores in the Shenhu area. South China Sea: Energy Rep. 8, 2936–2946.
Xu, J., Wu, S., Liu, J., Yuan, Y., Cui, J., Su, L., Jiang, X., Wang, J., 2021. New insights into controlling factors of pore evolution in organic-rich shale. Energy Fuels 35, 4858–4873.
Xu, L., Li, Q., Myers, M., Chen, Q., Li, X., 2019. Application of nuclear magnetic resonance technology to carbon capture, utilization and storage: a review. J. Rock Mech. Geotech. 11, 892–908.
Xu, Y., Lun, Z., Pan, Z., Wang, H., Zhou, X., Zhao, C., Zhang, D., 2022. Occurrence space and state of shale oil: a review. J. Petrol. Sci. Eng., 110183
Yan, W., Sun, J., Cheng, Z., Li, J., Sun, Y., Shao, W., Shao, Y., 2017. Petrophysical characterization of tight oil formations using 1D and 2D NMR. Fuel 206, 89–98.
Yan, W., Sun, J., Sun, Y., Golsanami, N., 2018. A robust NMR method to measure porosity of low porosity rocks. Microporous Mesoporous Mater. 269, 113–117.
Yang, F., Ning, Z., Liu, H., 2014. Fractal characteristics of shales from a shale gas reservoir in the Sichuan Basin. China: Fuel 115, 378–384.
Yao, Y., Liu, D., 2012. Comparison of low-field NMR and mercury intrusion porosimetry in characterizing pore size distributions of coals. Fuel 95, 152–158.
Yao, Y., Liu, D., Che, Y., Tang, D., Tang, S., Huang, W., 2010. Petrophysical characterization of coals by low-field nuclear magnetic resonance (NMR). Fuel 89, 1371–1380.
Yassin, M.R., Begum, M., Dehghanpour, H., 2017. Organic shale wettability and its relationship to other petrophysical properties: a Duvernay case study. Int. J. Coal Geol. 169, 74–91.
Yu, H., Wang, Z., Rezaee, R., Su, Y., Tan, W., Yuan, Y., Zhang, Y., Xiao, L., Liu, X., 2017. Applications of Nuclear Magnetic Resonance (NMR) Logs in Tight Gas Sandstone Reservoirs Pore Structure Evaluation: Unconventional Resources Technology Conference, pp. 119–127. Austin, Texas, 24-26 July 2017.
Yuan, Y., Rezaee, R., Al-Khdheeawi, E.A., Hu, S.-Y., Verrall, M., Zou, J., Liu, K., 2019. Impact of composition on pore structure properties in shale: implications for micro/mesopore volume and surface area prediction. Energy & Fuel 33, 9619–9628.
Yuan, Y.-J., Rezaee, R., Gu, J.-W., Wu, S.-T., Al-Khdheeawi, E.A., Wang, J., Pan, B., 2023. High-resolution coupling of stratigraphic 'sweet-spot'lithofacies and petrophysical properties: a multiscale study of Ordovician Goldwyer Formation. Western Australia: Petrol. Sci. 20, 1312–1326.
Yuan, Y., 2020. Multi-Scale Porosity and Pore Structure Assessment of Shale. Curtin University.
Yuan, Y., Rezaee, R., 2019a. Comparative porosity and pore structure assessment in shales: measurement techniques, influencing factors and implications for reservoir characterization. Energies 12, 2094.
Yuan, Y., Rezaee, R., 2019b. Fractal analysis of the pore structure for clay bound water and potential gas storage in shales based on NMR and N2 gas adsorption. J. Petrol. Sci. Eng. 177, 756–765.
Yuan, Y., Rezaee, R., 2019c. Impact of paramagnetic minerals on NMR-converted pore size distributions in Permian Caryngnia shales. Energy Fuels 33, 2880–2887.
Yuan, Y., Rezaee, R., Tongcheng, H., Verrall, M., Si-Yu, H., Jie, Z., 2018a. Pore Characterization and Fluid Distribution Assessment of Gas Shale: 80th EAGE Conference and Exhibition 2018, Unconventional Resources I (EAGE-SPE) (Copenhagen, Denmark).
Yuan, Y., Rezaee, R., Verrall, M., Hu, S.-Y., Zou, J., Testmanti, N., 2018b. Pore characterization and clay bound water assessment in shale with a combination of NMR and low-pressure nitrogen gas adsorption. Int. J. Coal Geol. 194, 11–21.
Yuan, Y., Rezaee, R., Yu, H., Zou, J., Liu, K., Zhang, Y., 2021a. Compositional controls on nanopore structure in different shale lithofacies: a comparison with pure clays and isolated kerogens. Fuel 303, 121079.

Yuan, Y., Rezaee, R., Zou, J., Liu, K., 2021b. Pore-scale study of the wetting behavior in shale, isolated kerogen, and pure clay. Energy Fuels 35, 18459–18466.
Zhang, B., Gomaa, A.M., Sun, H., Qu, Q., Chen, J.-H., 2014. A study of shale wettability using NMR measurements. Proceedings of the International Symposium of the Society of Core Analysts 8–11.
Zhang, J., Tong, Z., Niu, J., 2021. Exploration and exploitation progress of unconventional oil and gas in China. Advances in Resources Research 1, 13–19.
Zhang, J., Huo, Z., Tan, X., Liu, Y., Han, S., 2017. Shale gas geology in China. East China University of Technology Press, Shanghai.
Zhang, K., Kong, B., Zhan, J., He, R., Qin, T., Wu, K., Chen, Z., Chen, S., Zhang, J., 2016. Effects of Nanoscale Pore Confinement on CO2 Immiscible and Miscible Processes: SPE Low Perm Symposium.
Zhang, N., Zhao, F., Guo, P., Li, J., Gong, W., Guo, Z., Sun, X., 2018. Nanoscale Pore Structure Characterization and Permeability of Mudrocks and Fine-Grained Sandstones in Coal Reservoirs by Scanning Electron Microscopy, Mercury Intrusion Porosimetry, and Low-Field Nuclear Magnetic Resonance. Geofluids, 2018.
Zhang, T.-T., Li, Z.-P., Adenutsi, C.D., Wei, Y.-Z., Ma, Z.-F., You, Q., 2022. Quantitative Investigation of Nanofluid Imbibition in Tight Oil Reservoirs Based on NMR Technique: Petroleum Science.
Zhao, P., Wang, Z., Sun, Z., Cai, J., Wang, L., 2017. Investigation on the pore structure and multifractal characteristics of tight oil reservoirs using NMR measurements: Permian Lucaogou Formation in Jimusaer Sag. Junggar Basin: Mar. Petrol. Geol. 86, 1067–1081.
Zheng, S., Yao, Y., Elsworth, D., Liu, D., Cai, Y., 2020. Dynamic fluid interactions during CO2-ECBM and CO2 sequestration in coal seams. Part 2: CO2-H2O wettability. Fuel 279, 118560.
Zheng, S., Yao, Y., Liu, D., Cai, Y., Liu, Y., 2019a. Nuclear magnetic resonance surface relaxivity of coals. Int. J. Coal Geol. 205, 1–13.
Zheng, X., Zhang, B., Sanei, H., Bao, H., Meng, Z., Wang, C., Li, K., 2019b. Pore structure characteristics and its effect on shale gas adsorption and desorption behavior. Mar. Petrol. Geol. 100, 165–178.
Zhou, J., Liu, M., Xian, X., Jiang, Y., Liu, Q., Wang, X., 2019. Measurements and modelling of CH4 and CO2 adsorption behaviors on shales: Implication for CO2 enhanced shale gas recovery. Fuel 251, 293–306.
Zhou, J., Xie, S., Jiang, Y., Xian, X., Liu, Q., 2018. Influence of Supercritical CO2 Exposure on CH4 and CO2 Adsorption Behaviors of Shale: Implications for CO2 Sequestration. Energy & Fuels 32, 6073–6089.
Zhu, C., Sheng, J., Ettehadtavakkol, A., Li, Y., Gong, H., Li, Z., Dong, M., 2019. Numerical and experimental study of enhanced shale-oil recovery by CO2 miscible displacement with NMR. Energy Fuels 34, 1524–1536.
Zou, C., 2017. Unconventional Petroleum Geology. Elsevier.
Zou, J., Rezaee, R., Yuan, Y., Liu, K., Xie, Q., You, L., 2020. Distribution of adsorbed water in shale: an experimental study on isolated kerogen and bulk shale samples. J. Petrol. Sci. Eng. 187, 106858.
Ali, M., Al-Yaseri, A., Awan, F.U.R., Arif, M., Keshavarz, A., Iglauer, S., 2022. Effect of water-soluble organic acids on wettability of sandstone formations using streaming zeta potential and NMR techniques: Implications for CO2 geo-sequestration. Fuel 329, 125449.
Al-Khdheeawi, E.A., Mahdi, D.S., Yuan, Y., Iglauer, S., 2023. Influence of Clay Content on CO2-Rock Interaction and Mineral-Trapping Capacity of Sandstone Reservoirs. Energies 16, 3489.